J. Phys.: Condens. Matter 2 (1990) 1369–1412. Printed in the UK

REVIEW ARTICLE

The application of the specular reflection of neutrons to the study of surfaces and interfaces

J Penfold† and R K Thomas‡

† Neutron Science Division, Rutherford Appleton Laboratory, Chilton, Oxfordshire, UK

‡ Physical Chemistry Laboratory, Oxford University, South Parks Road, Oxford, UK

Received 26 June 1989

Abstract. The application of the specular reflection of neutrons to the study of surface and interfaces is described. The theoretical and experimental background to the technique is presented. A range of recent experimental results in surface chemistry, solid films and surface magnetism is discussed. In surface chemistry the results include adsorption of surfactants at the air–solution interface, insoluble monolayers and polymers at the air–liquid interface, soap films and adsorption at the liquid–solid and liquid–liquid interfaces. In solid films results on Langmuir–Blodgett films, hard carbon films, polymer films and some semiconductor layers are discussed. In surface magnetism experimental data which illustrate the nature of magnetism in magnetic multilayers and ferromagnetic films, and which describe flux penetration in superconductors, are presented.

1. Introduction

A range of phenomena analogous to those observed in classical optics are exhibited by slow neutrons; these include reflection, refraction and interference: see for example Klein and Werner [1]. Total reflection of slow neutrons was first reported by Fermi and co-workers [2, 3], and has since been extensively applied to a range of problems. Early applications of these phenomena have included the determination of scattering lengths [4], the production of neutron guides [5] and neutron spin polarisers [6–9].

The specular reflection of neutrons gives information on the neutron refractive index profile normal to an interface. The refractive index is simply related to the scattering length density and hence specular neutron reflection can provide important information about the composition of surfaces and interfaces. Similar information can be obtained using, for example, x-ray reflection. However there are many instances where the neutron method provides a distinct advantage. In contrast to x-rays, neutron scattering amplitudes vary randomly from element to element, and isotopic substitution can be used to produce large contrasts in the scattering density. Of particular importance is the large difference in scattering powers of hydrogen and deuterium; this has already been used to great effect in small-angle neutron scattering and will be seen to be of particular importance in surface chemistry. Due to the magnetic interaction, magnetic materials have a neutron spin-dependent refractive index, and the specular reflection of spin polarised neutrons is a sensitive probe of surface magnetism [10].

Since some of the early experiments [11–12] and applications [4–9], it is only relatively recently that any concerted effort has been made to apply the technique to the wider

0953-8984/90/061369 + 44 $03.50

study of surface and interfacial problems: this recent effort is highlighted by the work of Thomas *et al* [13–17] in the field of surface chemistry, and of Felcher [10, 18] in the area of surface magnetism. In the last few years the advent of dedicated spectrometers [19–22] has seen a rapid expansion in the scientific application of the technique to surface chemistry, solid films and surface magnetism (see for example work cited in reference [23]).

It is anticipated that with the development of new spectrometers and the widening of the range of applications the technique will undergo an expansion similar to small-angle scattering. It is, therefore, timely to review the current state of development of the technique, and present its possibilities to a wider community.

In the article we will discuss the theoretical background, describe experimental methods and illustrate the power of the technique with recent experimental examples drawn from the fields of surface chemistry, surface magnetism and solid films.

2. Theoretical background

The refraction and reflection of neutrons involves the interference between the incident neutron wave and waves scattered in the forward direction: these phenomena are in general independent of the atomic structure of the scattering material.

Goldberger and Seitz [24] have shown that the intensity of the reflected and transmitted neutrons follow the same law as electromagnetic radiation with the electric vector perpendicular to the plane of incidence; hence most of the standard formalisms in classical optics can be used with only minor modifications [25].

2.1. Refractive index

The refractive index at the boundary between two media is defined in the usual way as

$$n = k_1/k_0 \tag{2.1}$$

where k_1, k_0 are the neutron wavevectors inside and outside the medium. It is commonly written as

$$n = 1 - \lambda^2 A + i\lambda C \tag{2.2}$$

where $A = Nb/2\pi$, $C = N\sigma_a/4\pi$, N is the atomic number density, b is the bound coherent scattering length, σ_a is the adsorption cross section and λ is the neutron wavelength.

The refractive index for most media is less than unity, $(1 - n)$ being typically of the order of 10^{-6}, and as a result total *external* reflection is observed at very small critical glancing angles (in the region of milli-radians per Ångstrom).

From equation (2.2) it is noted that the refractive index is dispersive, and is strictly a complex quantity: the imaginary component is related to the absorption cross section and is usually negligible except for strong absorbers such as cadmium, samarium or gadolinium [26]. A detailed discussion of the definition of refractive index, the imaginary component and its relationship to refractive x-ray indices can be found elsewhere [27].

So far we have only considered the nuclear interaction: for magnetic materials there is an additional term in the refractive index to describe the magnetic scattering. For materials magnetised in the plane of the surface there is a spin-dependent refractive index $n_\pm$, for the neutrons polarised parallel (+) and antiparallel (−) to the applied field, and is given by

$$n_\pm = n_N \pm n_M = (1 - N\lambda^2/2\pi(b \pm C\mu)) \tag{2.3}$$

where μ is the average magnetic moment per atom and C is a constant equal to 0.2645×10^{-12} cm μB^{-1}.

2.2. *Specular reflection*

From Snell's law the critical glancing angle for total reflection is

$$\cos \theta_c = n \tag{2.4}$$

and, expanding the cosine for small θ (which is generally a sufficient approximation),

$$\theta_c/\lambda = (Nb/\pi)^{1/2}. \tag{2.5}$$

The specular reflection at the interface of two bulk media is described by Fresnel's law, where for $\theta \leqslant \theta_c$ the reflectivity R is unity and for $\theta \geqslant \theta_c$

$$R = \left| \frac{n_0 \sin \theta_0 - n_1 \sin \theta_1}{n_0 \sin \theta_0 + n_1 \sin \theta_1} \right|^2 \tag{2.6}$$

(see figure 1 for definition of symbols).

Considering the region of total reflection in more detail we can write

$$n_0 \cos \theta_0 = n_1 \cos \theta_1 \tag{2.7}$$

and hence

$$n_1 \sin \theta_1 = (n_1^2 - n_0^2 \cos^2 \theta_0)^{1/2}. \tag{2.8}$$

For $\theta \geqslant \theta_c$, then $n_1^2 \geqslant n_0^2 \cos^2 \theta_0$ and $n_1 \sin \theta_1$ is real. For $\theta \leqslant \theta_c$, then $n_1^2 \leqslant n_0^2 \cos^2 \theta_0$; and so $n_1 \sin \theta_1$ is imaginary (corresponding to an evanescent neutron wave), such that

$$n_1 \sin \theta_1 = -\mathrm{i}(n_0^2 \cos^2 \theta_0 - n_1^2)^{1/2}. \tag{2.9}$$

At the point of total reflection, $\theta = \theta_c$, $n_1 \sin \theta_1$ is identically zero, i.e. $n_1^2 = n_0^2 \cos^2 \theta_0$.

2.3. *Reflectivity profiles*

The essence of a neutron reflection experiment is to measure the specular reflection as a function of the wavevector transfer κ perpendicular to the reflecting surface. This can be related to the neutron refractive index profile normal to the interface, and is often simply related to the scattering length density, yielding information about the composition and density gradients of surfaces and interfaces.

A number of approximate methods to calculate reflectivity profiles exist, and can provide a good insight into the phenomenon. However, it is the standard multilayer optical methods [28, 29] that have been more extensively used so far. For discrete layers their application is exact, but they are also good approximations for boundaries which are not abrupt but which can be treated as a series of discrete layers with differing refractive indices.

For a single film on a substrate (see figure 2) the standard optical method gives an exact equation for the interference from the film, which is of the form [29]

$$R = \left| \frac{r_{01} + r_{12} \, \mathrm{e}^{2\mathrm{i}\beta}}{1 + r_{01} r_{12} \, \mathrm{e}^{2\mathrm{i}\beta}} \right|^2 \tag{2.10}$$

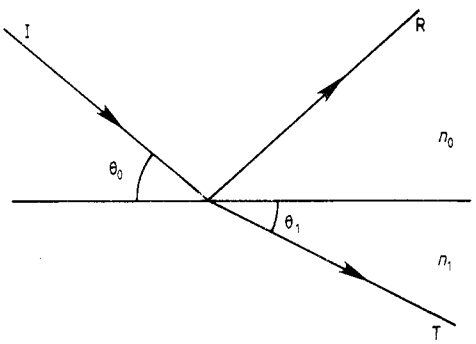

Figure 1. Interface between two bulk media of refractive indices n_0, n_1, showing the incident and reflected waves at an angle θ_0 and the transmitted wave at an angle θ_1.

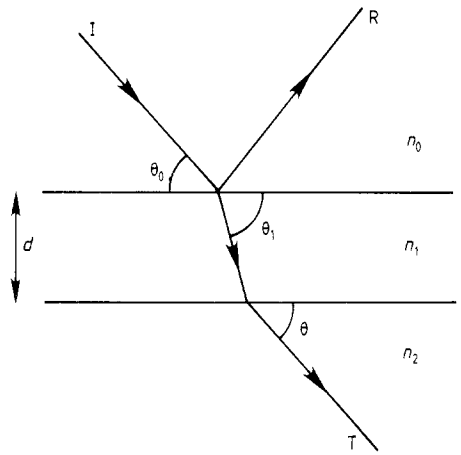

Figure 2. Thin film of thickness d and refractive index n_1 between two bulk media of refractive indices n_0, n_2.

where r_{ij} is the Fresnel coefficient at the ij interface, given by

$$r_{ij} = \frac{p_i - p_j}{p_i + p_j} \tag{2.11}$$

and $p_j = n_j \sin \theta_j$ and $\beta = (2\pi/\lambda)n_1 d \sin \theta_1$ (optical path length in the film).

This approach can be extended without too much difficulty to three or four discrete layers [30] but, beyond that complexity, a general solution must be adopted. Many of the early calculations were based on the standard method described in Born and Wolf [28], which by applying the condition that the wave functions and their gradients be continuous at each boundary gives a characteristic matrix for each layer such that for the jth layer

$$\mathbf{M}_j = \begin{bmatrix} \cos\beta_j & -(\mathrm{i}/p_j)\sin\beta_j \\ -\mathrm{i}p_j \sin\beta_j & \cos\beta_j \end{bmatrix}. \tag{2.12}$$

The resultant reflectivity for n layers is then obtained from the product of the characteristic matrices $\mathbf{M}_R = [\mathbf{M}_1][\mathbf{M}_2] \ldots [\mathbf{M}_n]$, by

$$R = \left| \frac{(M_{11} + M_{12}p_s)p_a - (M_{21} + M_{22})p_s}{(M_{11} + M_{12}p_s)p_a + (M_{21} + M_{22})p_s} \right|^2. \tag{2.13}$$

The optical matrix calculation gives the reflectivity profile from a model of the interfacial structure. The inversion of the reflectivity to give the structure is not possible. This will be discussed further below in connection with approximate methods.

2.4. Surface and interfacial imperfections

It is appropriate at this point to give some consideration to surface and interfacial imperfections. Beam divergence and long-range surface undulations, which can be considered as locally flat, contribute to the reflectivity profile in a similar way. If,

however, the surface is not entirely smooth its local roughness will modify the specular reflectivity in a manner similar to that of a diffuse interface (in terms of specular reflectivity the two are indistinguishable). The reflected intensity will be modified by a Debye–Waller-like factor of the form

$$I(\lambda) = I_0(\lambda) \exp(-q_0 q_1 \langle\sigma\rangle^2) \tag{2.14}$$

where $I(\lambda)$ and $I_0(\lambda)$ are the reflected intensity with and without surface roughness, $\langle\sigma\rangle$ is the root mean square roughness, and $q_0 = 2k \sin\theta_0$, $q_1 = 2k \sin\theta_1$.

Equation (14) is applicable to a bulk interface and has been derived by Névot and Croce [31] on the basis of a gaussian distributed height–height correlation function at the interface.

Figure 3 illustrates the application of Fresnel's law with a gaussian roughness factor to the reflectivity profile of a $\lambda/10$ optical flat: the full curve is a least-squares fit for an interfacial roughness of 32 Å.

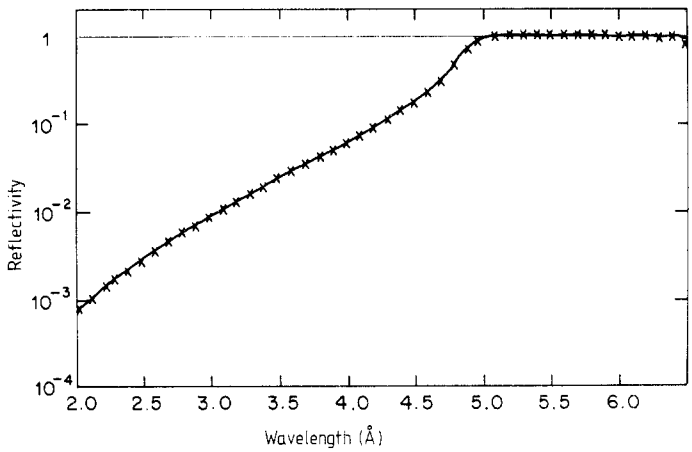

Figure 3. Reflectivity versus wavelength (for angle of incidence $\theta = 0.3°$) for a $\lambda/10$ optical flat: ×, data points; ——, a least-squares fit with scattering length density of the glass, $Nb = 0.36 \times 10^{-5}$ Å^{-2}, surface roughness = 32 Å and $\Delta\theta = 4.6\%$.

Cowley and Ryan [32] have extended this treatment of interfacial roughness to thin films in a consideration of the effects of roughened or diffuse interfaces on the specular reflection of x-rays from oxide layers in silicon. They have applied a gaussian roughness factor to each interface by modifying the Fresnel coefficients of equations (2.10, 2.11) such that

$$r_{ij} = \left(\frac{p_i - p_j}{p_i + p_j}\right) \exp[-0.5\,(q_i q_j \langle\sigma\rangle^2)]. \tag{2.15}$$

It has been shown [33] that this treatment of surface imperfection is equivalent to the matrix method (see equations (2.12), (2.13)) but with the interface divided into discrete layers with a gaussian distribution of density. It has the advantage, however, of being numerically much less unwieldly. It is therefore preferable to use an alternative multi-layer method to calculate reflectivity profiles, which will overcome this problem. One

such method is that of Abeles [29], which defines a characteristic matrix per layer in terms of Fresnel coefficients and phase factors, derived in optical terms from the relationship between electric vectors in successive layers. It is then possible to define a characteristic matrix per layer (analogous to equation 2.12):

$$\mathbf{C}_{\mathrm{M}} = \begin{bmatrix} \exp(\mathrm{i}\beta_{m-1}) & r_m \exp(\mathrm{i}\beta_{m-1}) \\ r_{\mathrm{m}} \exp(-\mathrm{i}\beta_{m-1}) & \exp(-\mathrm{i}\beta_{m-1}) \end{bmatrix}. \tag{2.16}$$

For N layers the matrix elements M_{11}, M_{21} of the resultant matrix $\mathbf{M}_{\mathrm{N}} = [\mathbf{M}_1][\mathbf{M}_2] \ldots [\mathbf{M}_{M+1}]$ give the reflectivity

$$R = M_{21}M_{21}^{*}/M_{11}M_{11}^{*}. \tag{2.17}$$

We can now conveniently introduce a roughened or diffuse interface at each boundary following Cowley and Ryan [32] (see equation (2.15)). This provides a convenient and closed form for calculating reflectivity profiles exactly [34] and is demonstrated by the fit to the reflectivity curve for a 10-bilayer cadmium docosanoate-d_{43} Langmuir–Blodgett film on silicon in figure 4 (see figure caption for details of the model).

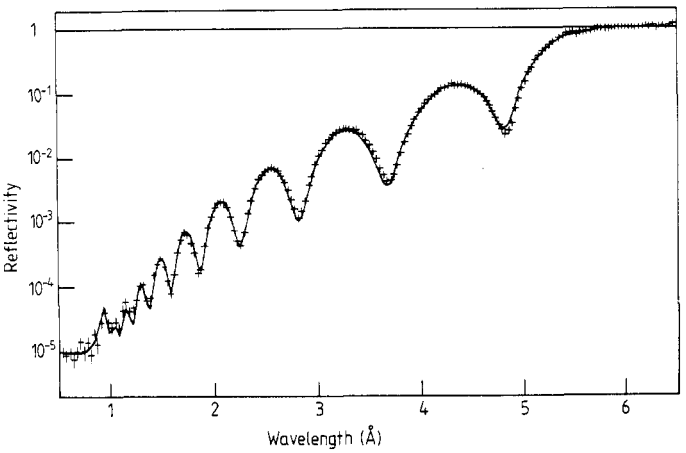

Figure 4. Reflectivity versus wavelength (for angle of incidence $\theta = 0.5°$) for a 10-bilayer cadmium docosanoate-d_{43} Langmuir–Blodgett film: + data points; —— a least-squares fit for a uniform single layer of thickness, $d = 565$ Å and scattering length density $Nb = 0.74 \times 10^{-5}$ Å^{-2}.

2.5. Magnetic effects

For magnetic materials, magnetised in the plane of the surface, the neutron spin-dependent refractive index gives rise to a neutron spin-dependent reflectivity, $R_{\pm}$. It has been shown [10, 18] that the neutron spin reflectivity ratio R^{+}/R^{-} provides a sensitive probe of the surface magnetisation profile.

For the simple three-medium system (see figure 2) it is straightforward to extend equation (2.10) to describe the spin-dependent reflectivities $R_{\pm}$ for a magnetic layer with a non-magnetic substrate such that

$$R_{\pm} = \left| \frac{r_{01\pm} + r_{12\pm} \exp(2\mathrm{i}\beta_{\pm})}{1 + r_{01\pm} r_{12\pm} \exp(2\mathrm{i}\beta_{\pm})} \right|^2 \tag{2.18}$$

and

$$\beta_{\pm} = (2\pi/\lambda)n_{1\pm}\, d \sin\theta_1. \tag{2.19}$$

It is clear that in the magnetic medium the phases of the neutron waves for each polarisation state are different, and this is the basic origin of the spin-dependent reflectivity.

2.6. Approximate methods

A number of approximate methods for calculating reflectivity profiles exist, which have not yet proved as useful for interpretation of experimental results as the exact simulations, but which can be used to give more insight into the factors determining the profile. Several methods have been described by Lekner [25], but the most useful is the kinematic (or first Born) approximation which has been applied to specular reflection by Crowley [35].

For weak elastic scattering in the kinematic approximation the differential scattering cross section is given by

$$I(\kappa) = \langle |\hat{\rho}(\boldsymbol{\kappa})|^2 \rangle \tag{2.20}$$

where $\rho(\boldsymbol{\kappa})$ is the Fourier transform of $\rho(\boldsymbol{r})$ over the whole sample:

$$\hat{\rho}(\boldsymbol{\kappa}) = \int_{-\infty}^{\infty} \exp(\mathrm{i}\boldsymbol{\kappa}\boldsymbol{r})\, \rho(\boldsymbol{r})\, \mathrm{d}\boldsymbol{r}. \tag{2.21}$$

For a macroscopic flat surface the specular component of the reflectivity, $R(\boldsymbol{\kappa})$, can be derived from equation (2.20) and is given by

$$R(\boldsymbol{\kappa}) = (16\pi^2/\kappa^2)|\hat{\rho}(\kappa)|^2 \tag{2.22}$$

where κ is now normal to the interface and $\rho(\kappa)$ is the one-dimensional Fourier transform of $\rho(z)$, the average scattering length density profile in the direction normal to the interface. An alternative expression, equivalent to equation (2.22), is in terms of $\mathrm{d}\rho/\mathrm{d}z = \rho^{(1)}$, and is

$$R(\kappa) = \frac{16\pi^2}{\kappa^4} |\hat{\rho}^{(1)}(\kappa)|^2. \tag{2.23}$$

There are three distinct types of interface to which these formulae may usefully be applied. The interface between a liquid and its vapour will usually show a smooth change in scattering length density across the interface. In this case we write

$$\hat{\rho}^{(1)}(\kappa) = \int_{-\infty}^{\infty} \exp(\mathrm{i}\kappa z) \left(\frac{\mathrm{d}\rho}{\mathrm{d}z}\right) \mathrm{d}z \tag{2.24}$$

which reduces to

$$\hat{\rho}^{(1)}(\kappa) = \int_{-\infty}^{\infty} \exp(\mathrm{i}\kappa z)\, \mathrm{d}\rho. \tag{2.25}$$

When $\kappa = 0$, we have

$$\rho^{(1)}(0) = -\Delta\rho_p \tag{2.26}$$

where $\Delta\rho_p$ is the contrast in scattering length density between liquid and vapour. We can now write the reflectivity in the form

$$R(\kappa) = R_p^0(\kappa)h^1(\kappa) \tag{2.27}$$

where

$$R_p^0 = (16\pi^2/\kappa^4)|\Delta\rho_p|^2 \tag{2.28}$$

and

$$h^1(\kappa) = \left|\frac{\hat{\rho}^{(1)}(\kappa)}{\hat{\rho}^{(1)}(0)}\right|^2 \tag{2.29}$$

and $R_p^0(\kappa)$ is the kinematic expression for the reflectivity of a sharp interface with a step in scattering length density of $\Delta\rho_p$ normal to the interface. Equation (2.28) is analogous to Porod's law in small-angle scattering.

$h^1(\kappa)$ is a normalised form factor which will modulate R_p^0 according to the width and shape of the interfacial region. When $\kappa \ll 1$, $h^1(\kappa) \sim 1$ and the surface profile appears to be sharp. Since total reflection occurs when κ is of the order of 10^{-2} Å^{-1}, the reflectivity profile close to the critical angle will appear to be that of the sharp interface unless the variation of $\rho^{(1)}(z)$ is over distances greater than about 10 Å. However, as κ increases the interfacial region is probed and $h^1(\kappa)$ starts to decay rapidly, causing $R(\kappa)$ to drop below the value $R_p^0(\kappa)$ for a sharp interface. The broader $\rho^{(1)}(z)$ the more rapid is the decay in $R(\kappa)$.

When κz is small, $\exp(i\kappa z)$ can be expanded in a Taylor series in powers of κz, giving

$$h^1(\kappa) \sim \exp(-\kappa^2\sigma^2) \tag{2.30}$$

for $\kappa\sigma < 1$, where σ is the standard deviation of $\rho^{(1)}(z)$. This equation corresponds to the Guinier approximation in small-angle scattering.

We now consider an isolated layer for which the scattering length density is the same on both sides of the layer, for example a soap film. We take the scattering length density to be zero except over the region of the film where it is $\rho_s(z)$. $R(\kappa)$ can now be expressed directly in terms of $\rho_s(z)$ using equation (22):

$$R(\kappa) = R_s^0(\kappa)h(\kappa) \tag{2.31}$$

where

$$R_s^0(\kappa) = \frac{16\pi^2}{\kappa^2}|m|^2 \tag{2.32}$$

$$h(\kappa) = \left|\frac{\hat{\rho}_s(\kappa)}{\hat{\rho}_s(0)}\right|^2 \tag{2.33}$$

and

$$m = \int_{-\infty}^{\infty} \rho_s(z)\,\mathrm{d}z. \tag{2.34}$$

$R_s^0(\kappa)$ is now the kinematic expression for the reflectivity of an infinitesimally thin film of scattering mass per unit area of m, and equation (2.32) is analogous to sheet scattering in small-angle scattering. Once again $h(\kappa)$ is a normalised form factor which modulates $R_s^0(\kappa)$. When κ is small $h(\kappa) \sim 1$, but when κ increases $h(\kappa)$ decays, resulting in the reflectivity falling below $R_s^0(\kappa)$.

Absorbed layers will in general have more complicated scattering length density profiles. We may write the scattering length density in the form

$$\rho(z) = \rho_s(z) + H(-z)\Delta\rho_p \tag{2.35}$$

where $H(-z)$ is the Heaviside function. Making use of the Fourier transform of the Heaviside function,

$$\int_{-\infty}^{\infty} H(-z)\exp(\mathrm{i}\kappa z)\,\mathrm{d}z = \pi\delta(\kappa) - \mathrm{i}\kappa^{-1} \tag{2.36}$$

together with equations (35) and (31), we obtain

$$R(\kappa) = R_0(\kappa) + R_1(\kappa)\Delta\rho_p + R_2(\kappa)\Delta\rho_p^2 \tag{2.37}$$

where

$$R_0(\kappa) = (16\pi^2/\kappa^2)m^2h(\kappa) \tag{2.38}$$

$$R_1(\kappa) = (32\pi^2/\kappa^3)S[\rho_s](\kappa) \tag{2.39}$$

and

$$R_2(\kappa) = 16\pi^2/\kappa^4 \tag{2.40}$$

where $R_0(\kappa)$ is the reflectivity of the surface film only and $R_2(\kappa)\Delta\rho_p^2$ (or R_p^0) is the reflectivity attributable only to sharp interface. The remainder, linear in $\Delta\rho_p$, results from cross-interference between the scattering from the sharp interface and that from the adsorbed layer. $S[\rho_s](\kappa)$ is the sine transform of ρ_s and is conveniently written in terms of a normalised form factor $s(\kappa)$, where

$$s(\kappa) = \kappa^{-1}\,S[\rho_s](\kappa)/\operatorname*{Lt}_{\kappa\to 0}\,(\kappa^{-1}S[\rho_s](\kappa)). \tag{2.41}$$

The denominator of equation (2.41) reduces to $\langle z\rangle m$, where m is as defined in equation (2.34) and $\langle z^n\rangle$ is the nth moment of ρ_s. Then R_1 can be written

$$R_1(\kappa) = (32\pi^2/\kappa^2)\langle z\rangle m s(\kappa). \tag{2.42}$$

Equations (2.37) and (2.40) show that measurements of $\Delta R\ (=R - R_p^0)$, the change in reflectivity upon adsorption, lead to information about the structure of the interfacial region. Approximations to R at both large and small values of κ illustrate the type of information that may be obtained. As before, Guinier approximations may be made at small κ, giving

$$h(\kappa) \sim \exp(-\kappa^2\sigma^2) \tag{2.43}$$

and

$$s(\kappa) \sim \exp(\langle z^3\rangle/3\langle z\rangle). \tag{2.44}$$

$s(\kappa)$ and $h(\kappa)$ will often be similar over a wide range of κ and indeed become equal for uniform layers and layers with exponential profiles. Thus at small κ measurements of ΔR lead to the amount adsorbed (m or $\langle z\rangle m$) and to the thickness of the layer (σ^2 or $\langle z^3\rangle/\langle z\rangle$).

$\rho_s(z)$ will often be a smooth function except for a step at $z = 0$. If this step is

$$\Delta\rho_s = \rho_s(0_+) - \rho_s(0_-) \tag{2.45}$$

then the large κ behaviour of R is given by

$$R(\kappa) \sim \frac{16\pi^2}{\kappa^4}(\Delta\rho_s - \Delta\rho_p)^2. \tag{2.46}$$

This is analogous to R_p^0 for a single sharp step of height $(\Delta\rho_s - \Delta\rho_p)$. Hence measurements of ΔR at large κ give the density of the adsorbed layer at $z = 0$. Other implications of the kinematic scattering formulae derived above are discussed by Crowley *et al* [36].

The kinematic theory has not been widely used to interpret data. However, examples of its applications are to the surface of liquids by Als-Nielsen [37], to polymer profiles at surfaces by Bouchaud *et al* [38], and to the structure of the surface of surfactant solutions by Lee *et al* [17]. The main deficiency of kinematic theory is that it fails to account for total reflection and is therefore not a good approximation near the critical angle. Its range of applicability has, however, been extended by Sinha *et al* [39] by using the distorted-wave Born approximation.

Felcher *et al* [18] have applied the approximate methods of Jacobsson [40], which describe the reflection from thin films with a continuously varying refractive index, to illustrate the enhancement of the spin-dependent reflectivity of a thin magnetic layer by the addition of a non-magnetic overlayer. A number of other approximate methods are described by Lekner [25] but they are mostly more suitable for reflection of light rather than neutrons.

2.7. Non-specular scattering

Specular reflection is determined by the mean scattering length density normal to the interface. Any fluctuations, either spatial or temporal, or a combination of the two, in the scattering length density will lead to non-specular or diffuse scattering. There have been many treatments of this phenomenon particularly for light or radar waves. A review of the phenomenon for light has been given by Lekner [25] and recent discussions of the relation between specular and non-specular scattering, particularly for x-rays, have been given by Sinha *et al* [39] and Braslau *et al* [41]. Braslau *et al* have considered the problem of distinguishing non-specular scattering from specular reflection from the surface of a liquid. This is important if density gradients at the liquid–vapour interface are to be distinguished from thermal fluctuations. This is discussed further in § 4. Sinha *et al* have analysed the distinction between scattering and reflection in more general terms and have also concluded that there is not necessarily any distinction between the two for a liquid surface.

One approach for elucidating the non-specular scattering from a liquid surface is to assume that the thermal fluctuations at the surface can be expanded in a Fourier series of capillary waves. The radiation is diffracted from these at angles away from the specular and with an intensity that depends on the Fresnel coefficients and the amplitude of the capillary waves. The specular/non-specular profile is then obtained by summing over all the capillary waves. To do this the amplitudes and spectral density of the capillary waves must be known. In practice this is determined over most of the wavevector range by the standard model of surface waves [25]. The difficulties are in the determination of the cut-offs at high and low wavevector. For x-rays and neutrons the latter will be determined by the resolution (of the order of microns). Litle is known about the behaviour of capillary waves at large wavevectors and it is necessary to make arbitrary assumptions, both about the cut-off in this part of the spectral range and about the

motion of the waves. A further difficulty with neutrons is that energy transfer between neutrons and surface excitations may become important at large wavevectors.

The non-specular scattering of neutrons from surface waves has been most elegantly explored by Hamilton *et al* [42], who have measured the diffraction of neutrons from a surface acoustic wave device. The surface excitation was periodic in the direction parallel to the neutron beam and the Doppler shifts of the neutrons by waves propagating with and against the beam were successfully distinguished (figure 5). The authors also made a complete analysis of the whole scattering process of neutrons from surface waves, albeit only from a one-dimensional excitation. The specular and non-specularly diffracted beams are shown clearly in figure 5 and their intensities agreed well with the theoretical prediction.

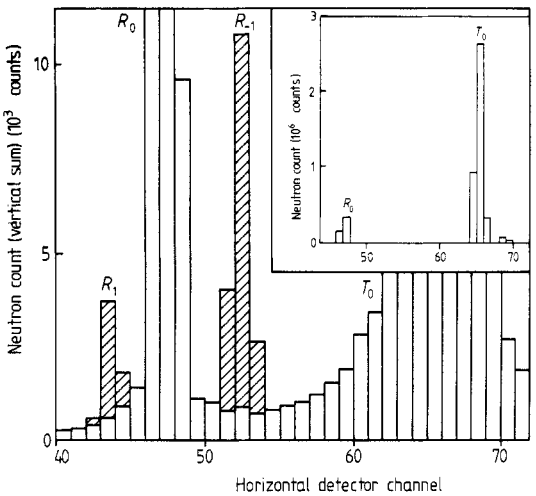

Figure 5. Specular reflection and non-specular diffraction from a surface acoustic wave device. The black areas are the difference in the signal when the SAW device is switched on. They are the diffraction peaks from the surface wave. The inset shows the transmitted and specularly reflected beams. The incident wavelength was 11 Å [42].

Many of the applications of neutron reflection, to be discussed in § 4, involve reflection from layered structures. On the other hand, most treatments of the effects of surface roughness have been confined to single surfaces. It is important in layer materials to allow for possible interference effects in the non-specular scattering. These have been observed in x-ray reflection from oxide layers on metal surfaces [43] and in light scattering from soap films [44]. In both cases the extra intensity gained by the non-specular component from the interference may contribute within the resolution of the experiment to the specular reflection. This would make any interpretation based only on specular reflection unreliable. Such a case is discussed in § 4. Models of non-specular scattering of this kind have been given by Vrij from light [44] and by Wainfan *et al* for x-rays [45].

3. Experimental methods

The objective of a specular reflection experiment is to measure the neutron reflectivity as a function of the wavevector transfer κ perpendicular to the reflecting surface. A wide

range of κ can be achieved either by using monochromatic beams and scanning a large number of angles, or by using the broad-band neutron time of flight (TOF) method to determine λ at fixed θ. As the critical glancing angles are small, narrow well collimated beams are required, and long-wavelength neutrons are used to maximise the reflection angles for a given κ.

Up to now the majority of the reactor-based measurements have been made using monochromatic long-wavelength neutrons and a θ (reflection angle)–2θ (detector angle) scan. The resolution in such measurements is determined by both angular ($\delta\theta$) and wavelength ($\delta\lambda$) spread. For fixed collimation ($\delta\theta$) and monochromatisation ($\delta\lambda$) the resolution varies with angle of incidence through a cot $\theta\delta\theta$ term. In this method the area of the sample illuminated also varies with θ, thus necessitating geometric corrections. However, a reactor-based reflectometer has potentially higher flux available at long wavelength, which may be important for measurements at particularly low κ, for studies of the liquid/solid interface, and when only a restricted range of κ is of interest. A second reactor–source method which is particularly advantageous for studying reflection around the critical angle is the gravity mirror method pioneered by Koester and Steyerl at Munich [4]. In this method, both θ and λ are varied, gravity being used to select the neutron wavelength.

An alternative way of carrying out the measurements is to use a fixed angle of incidence with a pulsed neutron beam and TOF to measure the wavelength. Some early TOF measurements were reported by Hayter *et al* [46]; and more recently Farnoux has developed a reactor based TOF [22] reflectometer. However, with the advent of pulsed neutron sources, the white-beam TOF method has become the natural way of performing reflectivity measurements and has been pioneered by Felcher [19] for magnetic studies. On pulsed neutron sources a fixed angle of incidence θ, with a wide wavelength band $\Delta\lambda$ and TOF analysis, offers many advantages. The fixed sample geometry ensures a constant sample illumination and the κ resolution is dominated by $\delta\theta$, being therefore essentially constant over the entire reflectivity profile. The contribution to $\delta\kappa$ from $\delta\lambda$ (or δt) is negligible compared with the angular uncertainty. The TOF methods also have the advantage that the reflectivity profile is measured simultaneously over a wide range of κ.

We will describe in more detail the major spectrometers on which the majority of the experimental data in the next section has been obtained; these are the CRISP reflectometer on the ISIS pulsed neutron source [20], and the D17 spectrometer at the Institut Laue–Langevin [47]. However, a number of other facilities now exist and include reflectometers at the Brookhaven reactor, at the IPNS at the Argonne Laboratory [19], Spear at Los Alamos [48], and the TOF instrument on the Orphée reactor at Saclay [22]. In addition other neutron laboratories have spectrometers in the planning stage, including Jülich [49], Delft [50] and NBS, Washington.

A schematic plan of the CRISP spectrometer [20], installed at the ISIS pulsed neutron source, is shown in figure 6. The instrument views the 20 K hydrogen moderator giving an effective wavelength range from 0.5 to 13 Å. The beam line is inclined at 1.5° to the horizontal and a horizontal slit geometry is employed, giving typical beam dimensions of 40 mm width and between 0.5 and 6 mm height. The final beam size and collimation is variable and is defined by two cadmium slits (S1, S2).

A single disc chopper (C) at 6 m from the moderator defines the wavelength band $\Delta\lambda$, and partially suppresses frame overlap contamination. A further suppression of long-wavelength frame overlap neutrons, which originate from earlier pulses than the primary reference pulse, is provided by the frame overlap mirrors (F) which are designed

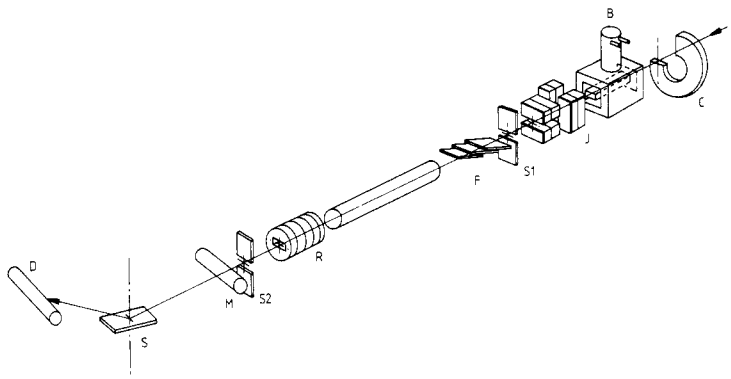

Figure 6. Schematic diagram of the CRISP reflector. C, chopper; B, beryllium filter; J, coarse collimating jaws; S1, S2, collimating slits; F, frame overlap mirrors; R, downstream collimation; M, neutron beam monitor; S, sample; D, detector.

to reflect out of the main beam wavelengths > 13 Å. The sample position (D) is located at 10.25 m from the moderator, and the sample to detector distance is 1.75 m. The detector is either a well-shielded and well collimated single He^3 gas detector or a one-dimensional multidetector with a positional resolution in either the vertical or horizontal plane of <1 mm.

The experimental arrangement is extremely flexible and solid films can be studied over a range of angles from ~0.15° to ~3°; liquid surfaces can be studied at angles <1.5° by the insertion of a supermirror. Particular features are the wide κ range available, the ability to study liquid surfaces and the capability to operate with high or low resolution $\delta\kappa$, low resolution having the advantage of much higher flux. A further demonstration of the flexibility of the spectrometer is shown in figure 7, which illustrates schematically the operation of the reflectometer in its polarised beam mode [21]. The incident beam polarisation is provided by a cobalt–titanium polarising supermirror (B); the polarising efficiency is ~99.950%, and the wavelength range is limited to a λ_{min} of 2.5 Å. The neutron spin flipper (C) is a Drabkin two-coil non-adiabatic spin flipper [51] which reverses the neutron beam polarisation over the whole wavelength band, with a wavelength-dependent efficiency of 98% at 2 Å and 87% at 7 Å. An appropriate static guide field (D) for the polarised beam is provided using permanent magnets.

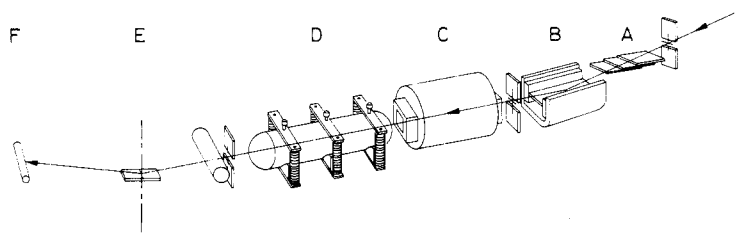

Figure 7. Schematic layout of the CRISP polarised beam reflectometer at the ISIS pulsed neutron source, Rutherford Appleton Laboratory. The principal components are: A, frame-overlap Ni mirrors set at a reflection angle $\theta = 1.3°$; B, a Co–Ti polarising supermirror; C, a two-coil non-adiabatic spin flipper; D, permanent magnet guide fields; E, the sample position; F, the neutron detector.

Although D17 at ILL has been used quite extensively to do reflection experiments, its normal use is as a small-angle scattering spectrometer. As such it is fully described in reference [47]. We describe here only those features which are relevant to its use as a reflectometer or which have to be modified when it is so used.

The machine is on a curved guide on the cold source of the reactor. The neutrons are monochromated by a velocity selector and the usable wavelength range is about 8.5 to 40 Å with a wavelength resolution of 5 or 10%. Because the wavelength is easily changed by changing the speed of the velocity selector, reflection experiments may be done by varying angle or wavelength, or more usually a combination of the two. The beam is in the horizontal direction with dimensions $30 \times 30\,\text{mm}^2$. It can therefore easily be collimated into a rectangular beam suitable for reflection experiments on either vertical or horizontal samples. The detector is a BF_3 multidetector consisting of 128×128 elements 5 mm apart in both directions. The distance between sample and detector can be varied over a wide range and, since the detector arm can be rotated through the angle 2θ, a wide range of momentum transfer can be covered, more than adequate for any reflection experiment on a vertical sample. For liquid samples the horizontal beam must be deflected down on to the liquid surface by means of a mirror and the liquid surface has to be lowered so as to be aligned correctly in the beam. In principle, more than one mirror may be used to increase the angular range of such an experiment. Then the range of momentum transfer is limited by the maximum angle of reflection that will just fall on the detector when it is placed as close to the sample as possible. At a wavelength of 8.5 Å κ_{max} is about 0.35 Å^{-1}. In practice, the higher background resulting from the use of the multidetector limits the accessible range of κ to reflectivities greater than about 2×10^{-6}. The only experiment so far done on a liquid surface was limited to momentum transfers less than 0.1 Å^{-1} [52].

There are a number of features of D17 which make it complementary to CRISP as a reflectometer. The large incident wavelength means that lower angles, and therefore lower momentum transfers, are more easily explored because a greater proportion of the incident beam may be used to illuminate the surface. The larger incident wavelength may also be an advantage for some experiments on the solid/liquid interface because a crystalline solid becomes transparent above the Bragg cut-off, which will be in the range of 4–7 Å for most materials of interest. Finally, although it is generally a disadvantage to have to measure the reflectivity point by point, in cases where it is sufficient only to know the reflectivity at a single value of the momentum transfer, the rate of data acquisition is much faster than on CRISP. This feature has been utilised by Lee [53] to study the rate of drainage of black soap films, where the thickness changes several hundred Å in tens of minutes.

4. Experimental results

In surface chemistry the initial scientific interest has been adsorption at the air–liquid interface of surfactants, fatty acids and polymers. In such systems, contrast variation gives the technique a powerful advantage over other surface probes: a point we will return to later in more detail. More recently the technique has been extended to adsorption at the solid–liquid interface.

For magnetic materials magnetised in the plane of the surface, the neutron spin-dependent refractive index gives rise to a neutron spin-dependent reflectivity $R_{\pm}$. The neutron spin reflectivity ratio R_+/R_- then provides a sensitive probe of the surface

magnetisation profile. The main areas of application have been in the study of magnetisation in ultra-thin ferromagnetic films, the nature of magnetism in multilayers, and the investigation of flux penetration in superconductors.

In solid films the advantages of neutron reflection are less obvious because x-ray reflection and other surface probes may often be more appropriate. However, a number of recent experiments have illustrated that in this area of surface science neutron reflection has some distinctive features which make it more effective in certain circumstances.

4.1. Surface chemistry

4.1.1. Pure liquids. The interface between a liquid and its vapour is usually described in terms of a diffuse layer in which the density falls from the density of the pure liquid ρ_1 to that of the vapour ρ_μ, and in terms of thermal fluctuations. The diffuse layer is characterised by its shape, which may have some functional form, and by its width, which we will refer to as the diffuseness of the interface. The thermal fluctuations will cause instantaneous vertical displacements at different parts of the surface, which will roughen the surface. Both diffuseness and roughness will contribute to an effective thickness of interface σ, and the reflectivity will fall below the ideal value for a perfectly smooth surface according to equations (2.27) and (2.30). It may be difficult to separate the two contributions in practice [41].

The only surface so far studied in any detail by neutron reflectivity is that of water. Penfold *et al* [54] have made a detailed study of the reflectivity of H_2O/D_2O mixtures, investigating the contribution of incoherent scattering to the background signal and studying the effect of temperature on the interfacial profile. Leaving aside the problem of separating the diffuseness and roughness of the surface of water, there are three main errors in the determination of the interfacial thickness. They are the level of background scattering, which limits the lowest reflectivity which can be measured, contamination by surface active impurities, and macroscopic vibrations of the surface. The effect of the latter may be reduced to an acceptable level, either by using devices that reduce vibrations at the sample position or, as used in [41], by using very thin films, in the region of 300 μm thick. Contamination is a serious problem in studies of the surface of water because of the high surface activity of most likely contaminants. Penfold *et al* [54] found that because most contaminants are proton containing they give rise to an extra incoherent background and therefore contamination can be monitored to a certain extent during neutron experiments on D_2O. The greatest limitation in the neutron experiment is the background arising from incoherent scattering, which is typically in the region of 10^{-6}. The interfacial thickness, defined as σ in equation (2.30), averaged over about twenty separate measurements at room temperature (20 °C), was found to be 2.8 Å, significantly smaller than the values of 3.3 ± 0.1 [41] and 3.8 Å [55] obtained by Braslau *et al* from x-ray measurements. There are three possible reasons for the discrepancy. Firstly, the measured thickness of the interface is sensitive to the resolution of the instrument because of the contribution of the thermal fluctuations, which do not all fall within the specular angle [41]. However, in this case the resolution of the neutron and x-ray experiments appears to be comparable. Secondly, most types of contamination, apart from electrolytes, will lower the surface tension. The mean square roughness, arising from capillary waves, is inversely proportional to the surface tension and therefore will be increased when the surface is contaminated. Also, as will be seen from the discussion below about the effects of surfactants on the reflectivity of D_2O,

contaminants will generally lower the reflectivity, causing an effective increase in the diffuseness of the interface. Thus the value of 2.8 Å determined by neutron reflection is only likely to be an upper limit. No attempt has yet been made to separate the two contributions to σ in a neutron reflection experiment.

4.1.2. Adsorption of surfactants at the air–solution interface. The specular reflection of neutrons is a powerful technique when applied to the study of adsorption at the air–solution interface. This largely results from the possibility of using isotopic substitution. Before considering how isotopic substitution experiments may be used it is worth reviewing the type of information available from traditional experimental techniques for studying adsorption at this interface. The main method has been to combine measurements of the surface tension and of the activity of one of the components using the Gibbs equation

$$d\gamma = -\Sigma\Gamma_i RT\, d\ln a_i \tag{4.1}$$

where $d\gamma$ is the change in surface tension when the activity a_i of component i is changed, and Γ_i is the surface excess of component i. For a two-component system, for example a surfactant in water, the equation becomes

$$d\gamma = -\Gamma_1 RT\, d\ln a_i - \Gamma_2 RT\, d\ln a_2 \tag{4.2}$$

which, with the introduction of the Gibbs–Duhem equation relating a_1 and a_2, becomes

$$d\gamma = -(\chi_2\Gamma_1/\chi_1 + \Gamma_2)RT\, d\ln a_2 \tag{4.3}$$

where χ is the mole fraction. It is clear from this equation that the two surface excesses Γ_1 and Γ_2 cannot be determined separately by means of such a measurement. The surface excess is defined relative to an arbitrary dividing surface, the Gibbs dividing surface. This is often chosen to be in a position such that there is no net excess of solvent. With this choice Γ_1 vanishes and equation (4.3) becomes

$$d\gamma = -\Gamma_2^1 RT\, d\ln a_2 \tag{4.4}$$

where the superscript denotes that the surface excess of solute is being measured relative to the particular Gibbs plane for which Γ_1 is zero.

The discussion above shows the shortcomings of the surface tension method. No structural information is obtained either about the configuration of the individual surfactant molecules or about their configuration in relation to the solvent. A further important difficulty arises for solutions of surfactants at and above the critical micelle concentration (CMC). Figure 8 shows the variation of surface tension with concentration for sodium dodecylsulphate (SDS) [56]. Below the CMC the negative slope, which gives Γ_2^1, is reasonably constant over a range of concentration, showing that the monolayer is completed well below the CMC. Above the CMC the slope of the graph is much more gradual. This does not necessarily indicate an abrupt change in the amount adsorbed, because above the CMC both the surface tension and the activity of the surfactant change only slowly with concentration, the latter because of the micelle monomer equilibrium. These small changes are difficult to measure and equation (4.4) loses much of its effectiveness.

A more direct method than measurement of surface tension involves the use of radiotracers [57]. The experiment is straightforward in principle, a scintillator probe being placed close to the surface to detect the amount of radioactively labelled surfactant at the surface. In practice, the accuracy depends on the penetration of the radiation and

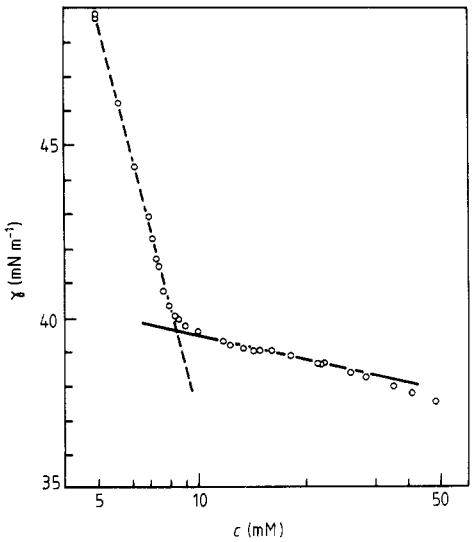

Figure 8. The variation with concentration of the surface tension of sodium dodecyl sulphate solutions in water. The critical micelle concentration is at the intersection of the two straight lines at 0.008 M [56].

will become less good as the concentration of the solution is increased. However, below the CMC the accuracy is high and compares well with the surface tension method. However, once again, the technique yields no structural information.

Since neutron reflection is related to the refractive index profile normal to the surface and since the refractive index profile is directly related to the composition profile, it is clear that the specular reflection technique can be used to obtain both the amount adsorbed and structural information about the layer. The quality of the information depends on the resolution of the experiment and the ability of the experiment to highlight the adsorbed species. The variation of neutron scattering lengths between isotopes makes it possible not only to highlight particular parts of the surface but even to eliminate altogether the reflection from anything other than the surface region.

Since the majority of surface chemical systems contain protons in at least one of the components, and because the scattering lengths of protons and deuterons are opposite in sign, H/D substitution has been widely used to change the contrast in neutron scattering experiments. In the reflection experiment it is possible to choose the H/D ratio for many solvents so that there is no specular reflection at all. For example the mole ratio of D_2O in H_2O required to produce null reflecting water is 0.088. The total neutrons scattered on to a multidetector from the surfaces of D_2O and null scattering water are shown in figure 9, from which it can be seen that the intensity of the specularly reflected beam from null reflecting water is indeed negligible and must be less than the background scattering, i.e. less than about 10^{-5} in the configuration shown in figure 9.

Thus, apart from the background scattering, which is easily subtracted, there is no signal at all from a null reflecting solvent. It is often relatively easy to make the homogeneous solution also null reflecting. In the case of many surfactants the concentration range of interest is sufficiently low that the solution is approximately null reflecting, even when the solute is fully deuterated. If adsorption occurs, however, there will be reflection and it will depend entirely on the surface layer. Thus the technique can be made specific to the adsorption of the solute. Furthermore, it will often also be possible to use H/D substitution to eliminate reflection from the solute. In this way the

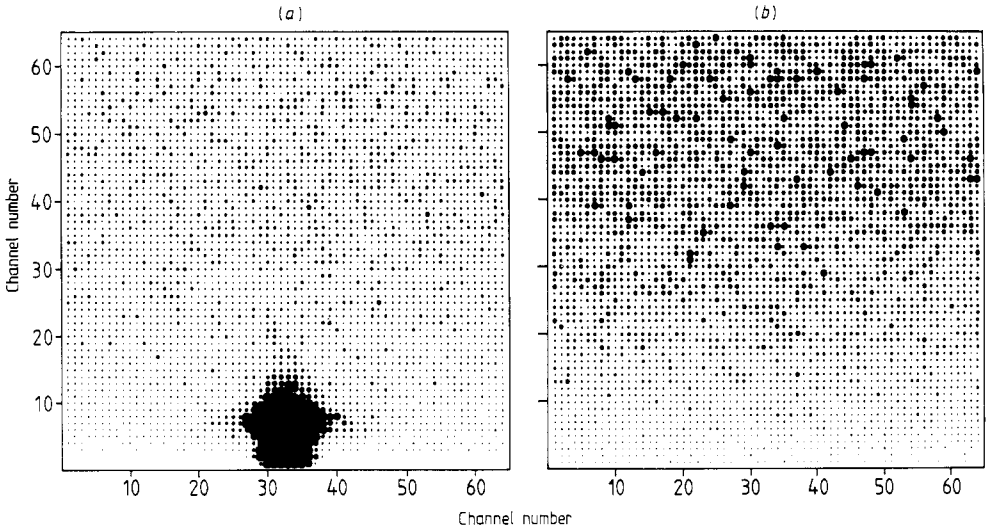

Figure 9. Neutron scattering patterns registered on a multidetector for (*a*) D_2O and (*b*) null reflecting water (0.088 mole fraction fraction of D_2O in H_2O). The dots in increasing order of size represent intensities in 100 count intervals from 0 to 800. The completely full points represent intensities greater than 800. The specular reflection peak of D_2O reaches a maximum of 24 4000 counts. The specular reflection is for a momentum transfer of 0.036 $Å^{-1}$ (κ_c is 0.017 $Å^{-1}$ for D_2O) [52].

profile of the solvent at the surface may be studied in an independent experiment, thus overcoming the problems arising from equation (4.3) in surface tension measurements.

Isotopic substitution may also be used to highlight particular parts of the solute molecule by selective substitution. Once again, H/D substitution is useful but when it comes to highlighting, say, the distribution of counter-ions at the boundary between a charged monolayer and the bulk solution, a whole range of different isotopic substitutions becomes possible, e.g. $^{35}Cl/^{37}Cl$, as used in the determination of the structure of the hydration shell of the chloride in aqueous solution [58]. We now consider some examples of the application of isotope substitution in the determination of the structure of the surfaces of surfactant solutions.

Figure 10 shows neutron reflectivity profiles, after subtraction of the incoherent background, of three isotopic species of decyltrimethylammoniumbromide (DTAB) at the same concentration in null reflecting water [17]. The concentration is such that there is a monolayer of surfactant at the surface. The three isotopic species are the fully deuterated (dDdTAB) chain deuterated (dDhTAB) and head group deuterated (dDdTAB). The overall level of the scattering is approximately determined by the total excess scattering length density in the surface region and this decreases with the number of deuterium atoms in the three species. Where the signal is strong, as for the first two species, the difference in slope of the two curves in this region also shows that the reflecting layers have different thicknesses. This immediately shows that the molecules are oriented at the surface. If they were just randomly oriented, the scattering length density of the layer would change with the number of deuterium atoms but its thickness would not. A more detailed analysis where a single structure was fitted to the three sets of data shown in figure 10 gave the monolayer structure shown in figure 12(*a*).

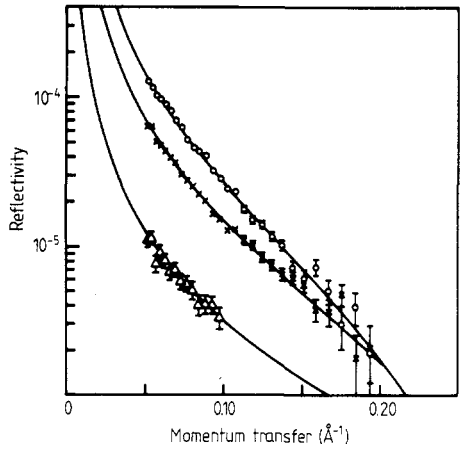

Figure 10. Observed and calculated specular reflectivity profiles of isotopic species of 0.05 M decyltrimethylammonium bromide (DTAB) in null reflecting water (background subtracted). In order of decreasing reflectivity the isotopic species are dDdTAB, dDhTAB and hDdTAB. The continuous curves are profiles calculated for the structure shown in figure 12(*a*) [17].

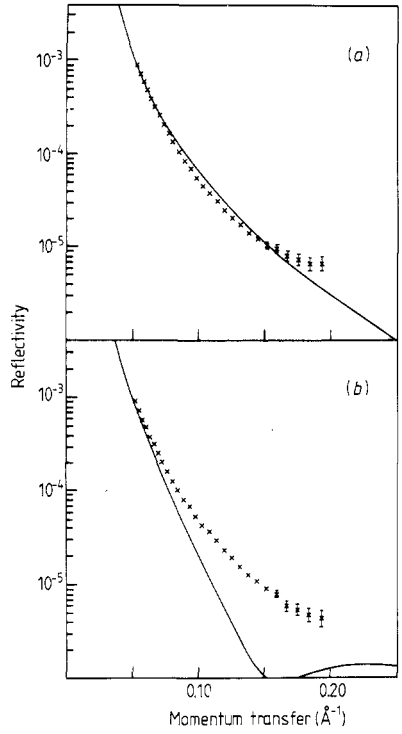

Figure 11. Calculated and observed specular reflectivity profiles of a 0.05 M solution of fully protonated DTAB in D_2O (background subtracted). The calculated profiles are (*a*) for water in the head group region only (the structure in figure 12(*c*)); and (*b*) for water filling the empty space in both head group and chain regions [17].

To examine the distribution of the solvent at the surface it is necessary to contrast out the solute while maximising the scattering length density of the solvent. For DTAB this is approximately achieved simply by using the fully protonated species in D_2O. The reflectivity in this case (figure 11) is somewhat lower than that of D_2O. To deduce where the water is in relation to the surfactant now requires a little more analysis. The area occupied per surfactant molecule and the thickness of the surfactant layer are determined from the reflectivity measurement on the fully deuterated species and, in conjunction with an approximate estimate of the volume of the molecule [59], give the volume fraction of the surfactant in the layer. The remainder of the layer can only consist of water, counter-ions and empty space (air). Figure 11 shows profiles calculated for the two cases of no empty space and a fraction of empty space corresponding to the chain region of the monolayer only. The difference between the two profiles is large and it is clear that only the latter fits the observed profile. By fitting a single chemical model to the whole set of measurements at different contrasts, Lee *et al* [17] were able to deduce the structure of the adsorbed layer shown in figure 12(*c*).

In the example above isotopic substitution was used in a simple way to demonstrate how independent information about solute and solvent could be obtained by contrasting

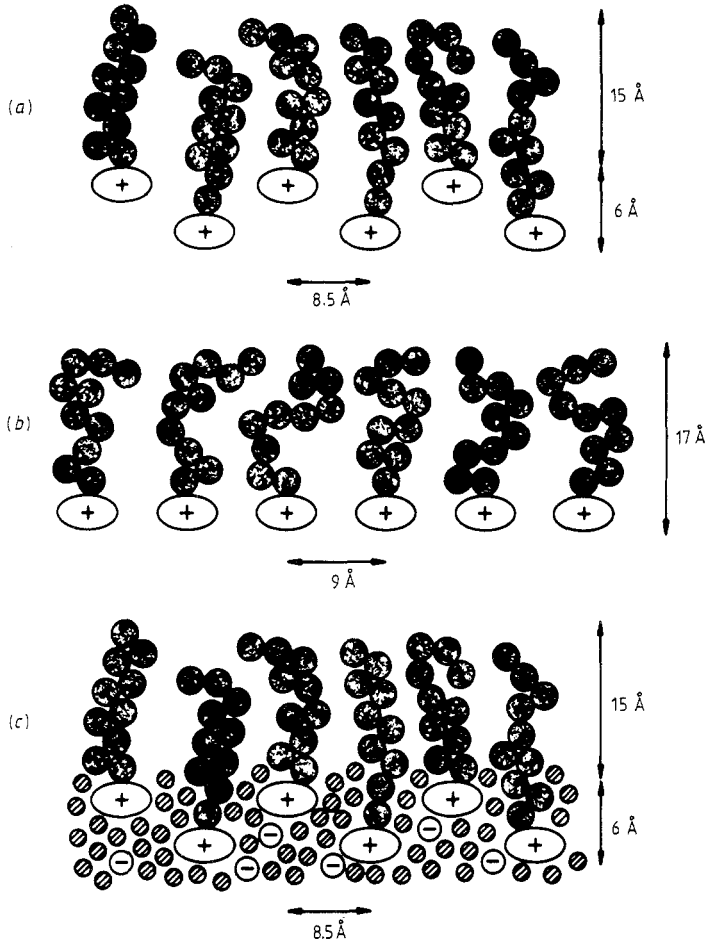

Figure 12. The distribution of water and DTAB molecules at the air–solution interface. The configuration of DTAB molecules within the adsorbed layer is shown at (*a*) 0.05 M and (*b*) 0.01 M or less. (*c*) Full structure of the layer at 0.05 M deduced from isotopic substitution measurements [17].

out one of the species. The same method may be used to examine the adsorption of one solute species in the presence of another. The simplest example to illustrate this is of a charged surfactant and its counter-ion. In terms of equation (4.1) there are two distinct total surface excesses, which will be identical because of electron-neutality. However, their distributions in the surface region will be quite different. Penfold *et al* [60] have investigated the system tetramethylammonium dodecylsulphate (TMDS) in water. The reflectivity of the combination of protonated surfactant chain and deuterated counterion (dTMhDS) in null reflecting water results only from the excess counter-ions at the surface and is shown in figure 13 for the monolayer. As for the determination of the distribution of the solvent at the DTAB–air interface, some analysis is necessary to deduce anything from the profile of figure 13. The area per molecule and hence the number of counter-ions per unit area was determined from the reflectivity of the species with fully deuterated chains in null reflecting water. Likely distributions for counter-ions at the surface are in

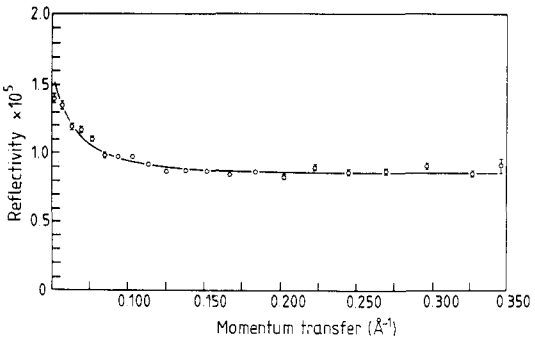

Figure 13. Observed and calculated reflectivity profiles for dTMhDS in null reflecting water at 0.005 M (background not subtracted). The continuous line is calculated for 25% of the ions bound in a Stern layer and the remainder in a diffuse layer within a gaussian distribution of half-width 42 Å, the Debye length at this concentration [60].

a monolayer immediately adjacent or incorporated with the head group of the surfactant (Stern layer), in a diffuse double layer, or in some combination of the two. Calculations for these different models show that the data are consistent with a fraction of about 0.25 of counter-ions in the Stern layer with the remainder in a diffuse layer with thickness approximately equal to the Debye length $1/\kappa$.

The nature of adsorption from mixtures of surfactants has been relatively little studied because the Gibbs equation becomes rather cumbersome to apply. A classical problem in surface tension measurements is the minimum in the surface tension often observed in the sodium dodecyl sulphate (SDS) water system, which arises from the presence of small amounts of the impurity dodecanol. Docecanol is almost insoluble in water and on its own forms a close-packed monolayer on the surface. Thus a very small amount in an SDS solution below the CMC will preferentially adsorb at the surface. Above the CMC the SDS solubilises the dodecanol and removes it from the surface. Since the surface free energy of a monolayer of SDS is greater than one containing a proportion of dodecanol, the surface tension will then rise at the CMC. In principle equation (4.2) may be used to determine independently the surface excesses of SDS and dodecanol, but the determination of the activity of the latter is not easy. Figure 14 shows how easy it is to measure the dodecanol concentration by reflectivity. Figure 14 shows the reflectivity of SDS (protonated) in null reflecting water and, as would be expected, since both surfactant and water are contrast-matched to air, there is no reflectivity. On the other hand the spread monolayer of pure deuterated dodecanol gives a strong reflected signal. The addition of a trace amount of deuterated dodecanol in the system leads to a significant increase in the reflectivity because the dodecanol displaces SDS from the monolayer. The

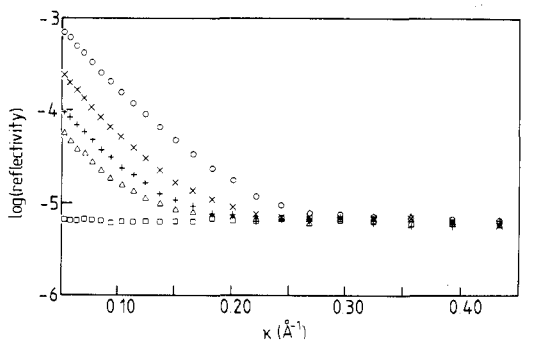

Figure 14. Reflectivity profiles of deuterated dodecanol–sodium dodecyl sulphate (SDS)–null reflecting water mixtures (background not subtracted) [61]. Circles show the profile of a spread monolayer of deuterated dodecanol on null reflecting water; squares show the reflectivity of 0.009 M SDS in water. The remaining three profiles are for 1.25% dodecanol in SDS and a varying SDS concentration of 0.00675 M (×), 0.009 M (+) and 0.012 M (△). The CMC is 0.008 M.

actual amount has been determined over a wide range of conditions, leading to a set of isotherms of dodecanol under conditions of constant SDS concentration [61].

Above the CMC it becomes more difficult to determine the total surface excess with any accuracy from equation (4.1) because both $d\gamma$ and $d\ln a$ are very small. Not only is there uncertainty about the total surface excess; nothing at all is known about the structure of the surfactant. Lee *et al* [17] found that above the CMC the reflectivity of protonated decyltrimethylammonium bromide (hDhTAB) in D_2O was unexpectedly higher than that of D_2O. Since the scattering length density of the surfactant is close to zero the mean scattering length density of the solution must be lower than D_2O and a simple monolayer of surfactant had already been shown to lower the reflectivity, as expected. The increase in the reflectivity is most clearly shown by plotting the ratio of the reflectivities of surfactant solution to that of pure D_2O, and is shown in figure 15.

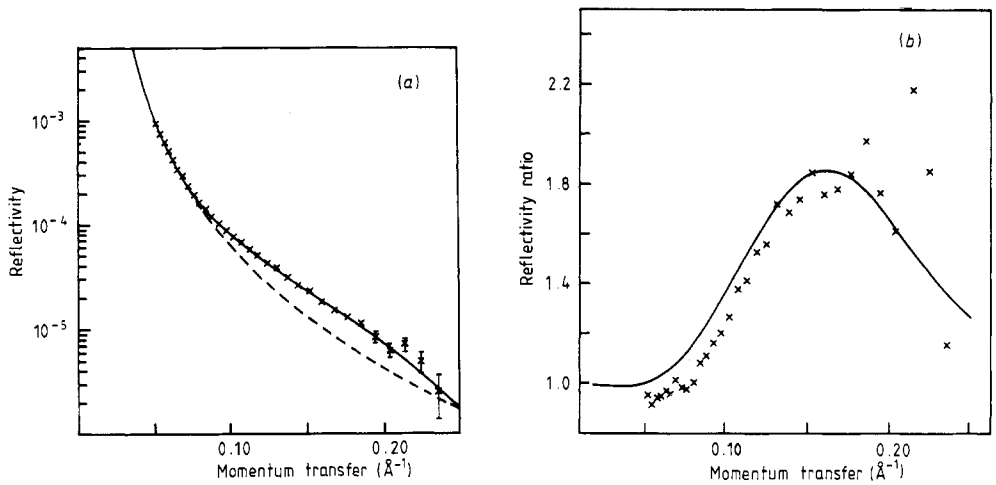

Figure 15. (*a*) Observed and calculated specular reflectivity profiles of a 0.1 M solution of fully protonated DTAB in D_2O. The calculated profile is for the interfacial structure with a dense layer of water. (*b*) Ratio of the observed reflectivity in (*a*) to the calculated reflectivity for perfectly smooth D_2O. The continuous line is for the same structure as used for (*a*) [17].

The reflectivity ratio, which equations (2.38) to (2.41) show to be closely related to the form factor of the inhomogeneity at the surface, goes through a maximum of close to 2 at a momentum transfer of about 0.16 Å^{-1}. Such an increase can be caused in two ways. Either there is a layer of D_2O of anomalously high density or there is some sort of layered structure of surfactant beneath the monolayer that forms the actual surface. The first interpretation concluded that there must be a layer of 'anomalous' water [17] which gives a deceptively good fit to the data as shown in figure 15. Subsequent experiments have demonstrated the phenomenon for trimethylammonium bromides with different chain lengths (see figure 16) and for the sodium alkyl sulphates [62]. The later results show that the maximum in the reflectivity ratio is an interference effect. Its position depends on the chain length of the surfactant and its intensity is largely determined by the volume fraction of the surfactant. Whilst an accurate structure has not yet been determined, two features which appear necessary to produce such an effect are a high contrast between the surfactant layers and D_2O and a spacing of the layers which varies

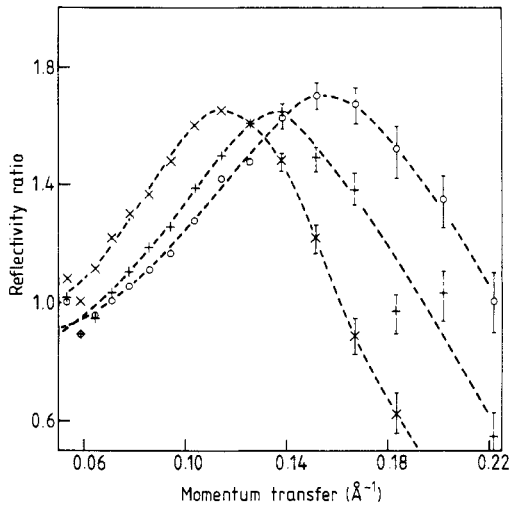

Figure 16. The observed ratios of the reflectivities of solution of alkyl trimethylammonium bromides (CTAB) to the calculated reflectivity of perfectly smooth D_2O. The concentrations were 0.1 M for C_{10}TAB (○), 0.051 M for C_{12}TAB (+) and 0.0385 for C_{14}TAB (×). The broken curves are to guide the eye [62].

over quite a wide range. The first feature suggests that the layers closest to the surface have a lamellar structure. This would be surprising if confirmed, because the overall surfactant concentrations were less than 5% by volume whereas the lamellar phase in these systems is generally not formed until this concentration reaches about 50% by volume.

4.1.3. Insoluble monolayers. As the hydrocarbon chain length of a surface active molecule is increased it will become less soluble. If its solubility is sufficiently low, or if its rate of solution is sufficiently slow, it may be possible to spread it as a monolayer on the surface of water. In fact, a wider variety of compounds than just surfactants will form spread monolayers, including polymers whose monomer segments are themselves insoluble. The specific interactions that determine whether or not a given species will spread are not yet well understood. Spread monolayers are the precursors in the formation of Langmuir–Blodgett films and it is therefore important to understand their structure and properties, particularly those factors which affect film deposition. The traditional method of study of monolayers has been by means of surface pressure (π)–area (A) isotherms, which often reveal a complicated phase diagram [63]. As with the adsorbed surfactant layers, the only experimental techniques capable of determining directly the structural parameters of such layers are x-ray and neutron reflectivity.

The first study of an insoluble monolayer by neutron reflection was by Bradley *et al* [16], who reported results obtained on the gravity mirror for layers of fully deuterated butyl arachidate (n-butyl eicosanoate; $C_{19}D_{39}CO_2C_4D_9$) at varying surface pressure. The range of momentum transfer accessible on the gravity mirror is small, so the information obtained was somewhat limited. The results do, however, illustrate an important aspect of the reflectivity technique. It was not possible over the range of momentum transfer used to determine separately the thickness of the layer and its composition. In this respect a reflectivity measurement at small values of $\kappa\sigma$, where σ is the thickness of the layer, is somewhat equivalent to an ellipsometric measurement where what is actually determined is the optical path length. Further assumptions are then needed to separate thickness and composition.

A more complete study of a spread monolayer of docosanoic acid ($C_{21}D_{43}COOH$) has been made by Grundy *et al* [64], who used both x-ray and neutron reflectivity to

study the monolayer over a range of surface pressure and pH. The contrast between the hydrocarbon part of the monolayer and the subphase is small for x-rays and the thickness of the layer could not therefore be determined unambiguously from the x-ray reflectivity. On the other hand x-rays are extremely sensitive to the number of bound groups of the layer and particularly to the number of bound Cd^{2+} counter-ions. The neutron results showed that in the condensed phase the molecules are perpendicular to the surface, and that the thickness of the hydrocarbon tail is equal to the extended length of the chain. At low surface pressures where the monolayer is in an 'expanded' phase the molecules were found to tilt by about 30° if the pH was low enough for cadmium ions to be entirely displaced from the layer. The change in thickness is clearly demonstrated by a shift in the peak of the reflectivity ratio (as described in the previous section) plotted in figure 17. The peak in the form factor of the density profile through the monolayer shifts to a higher value of momentum transfer as the layer becomes thinner. At higher pH, where the acid has changed to the cadmium salt, the molecules remain perpendicular to the surface in the expanded phase. The most unexpected result of this work was the finding that the molecules form islands on the surface in the expanded phase rather than spreading uniformly over the surface.

4.1.4. Polymers at the air–liquid interface. The configuration of polymers at the air–solid interface has long been of considerable interest, both because it presents a theoretical challenge and because of its practical importance in the steric stabilisation of colloids. When a polymer is adsorbed at a surface the energy gained from the binding of the segments to the surface is offset by the loss of configurational entropy in the more restricted configuration of the adsorbed polymer. The most important experimental quantity is then the segment density profile normal to the surface. Although there have been a limited number of experiments done on the structure of polymers at the solid–liquid interface (for a review see [65]), there have been few experiments of any kind on the adsorption of polymers from solution at the air–solution interface. However, there

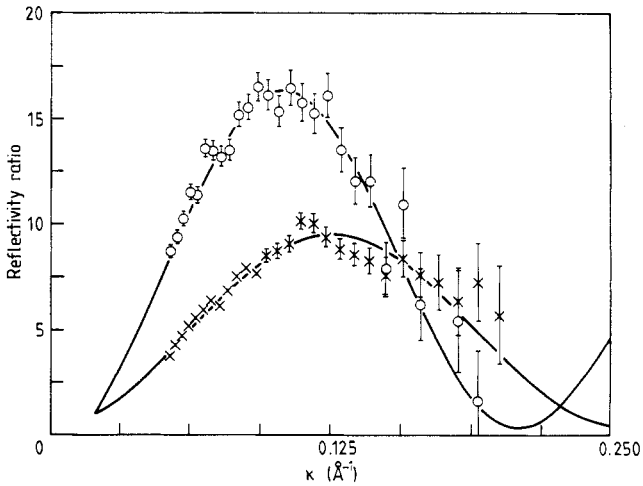

Figure 17. The ratio of the observed reflectivity (background subtracted) to the reflectivity of the perfectly smooth subphase (1:1 $D_2O:H_2O$) for deuterated docosanoic acid on a pure aqueous subphase at pH = 3.2 and a surface pressure (π) of 35 mN m^{-1} and no added cadmium (○), and for a 2.5×10^{-4} M $CdCl_2$ solution at pH = 3.2 and a surface pressure less than 2 mN m^{-1} (×) [64].

have been a number of measurements of π–A isotherms of insoluble monolayers of both homo- and co-polymers, for example [66]. Whilst such measurements are important for characterising many features of the layer, they have the drawback that they can give no information about the structure of the layer. Specular reflection is ideally suited for determining the segment density profile normal to the surface.

Rennie *et al* [52] have studied the surface of polyethylene oxide (PEO) of molecular weight 20 000 in solution in water, using contrast variation to highlight either the polymer or the solvent at the air–solution interface. Water is a good solvent for PEO at room temperature, but as the temperature is increased or as electrolyte is added it becomes less good, reaching a θ point at the combination of 45°C and 0.4 M $MgSO_4$. Experiments in null reflecting water were used to measure the total amount of PEO adsorbed as a function of concentration and quality of the solvent. In mean field models of polymer adsorption, the adsorption is characterised by an adsorption parameter χ_s and a solvent interaction parameter χ, together with the number of statistical segments in the chain [67]. The variation of the amount adsorbed with solvent quality was satisfactorily explained by mean field theory; the variation with concentration less so. The most important discrepancy between experiment and theory was that, with χ_s determined from the total amount of polymer adsorbed, the predicted mean field segment density profile (figure 18(*a*)) gave a totally unsatisfactory fit to the reflectivity profile (figure 18(*b*)). An alternative prediction of the segment density profile from scaling theory was no more successful. The fit of a single model to the data from two isotopic compositions

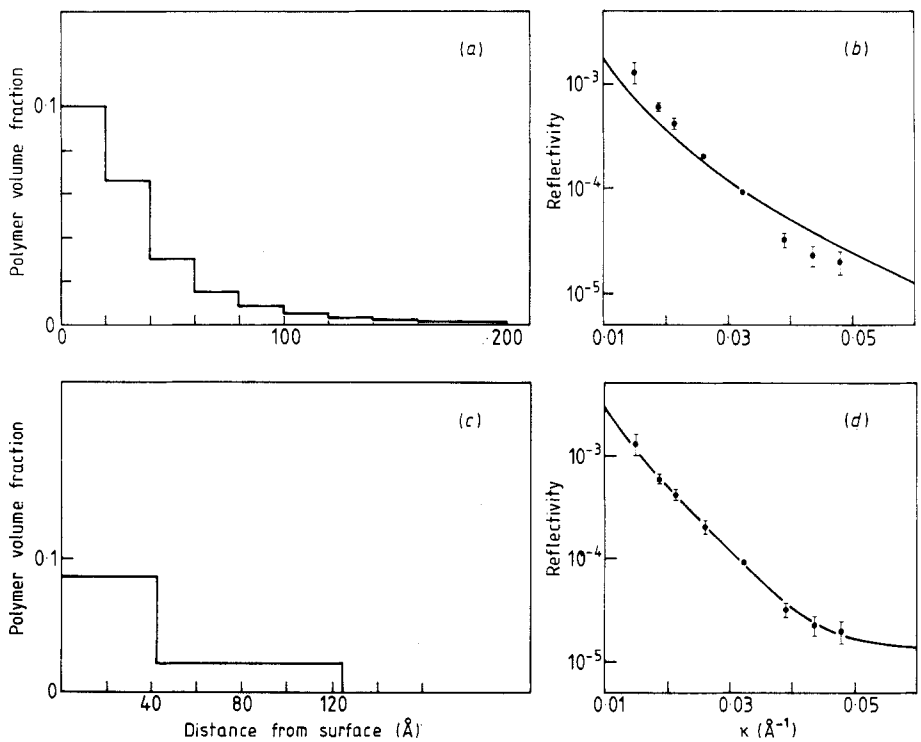

Figure 18. Observed and calculated reflectivity profiles from the air–solution interface of a 0.1% by weight solution of deuterated polyethylene oxide (M_n = 19 600) in null reflecting water (background subtracted). (*b*) Profile calculated for the mean field distribution shown in (*a*). (*d*) Profile calculated for the distribution shown in (*c*) [52].

gave the segment density profile shown in figure 18(*c*) and the fit to the reflectivity profile shown in figure 18(*d*). Whilst the profile shown in figure 18(*d*) is clearly physically unrealistic in the sense that it would be expected to be a smooth distribution, it is the minimum description necessary to fit the data. Rennie *et al* show that the most likely realistic distribution in the 'tail' part of the profile in figure 18(*c*) is a half-gaussian. Another conclusion from the experiment was that the surface is roughened by the polymer on a scale comparable with the statistical segment length, about 21 Å for PEO. This should be compared with the roughness of about 3 Å for the pure water surface.

PEO in water shows a number of peculiarities which make it an unsuitable system from which to draw any general conclusions. Sun *et al* [68] have studied a system likely to be of more general interest: polydimethyl siloxane (PDMS) in toluene. This system has already been well studied by surface tension measurements and the surface tension, and hence total amount adsorbed, varies with concentration in accordance with scaling law predictions [69]. Sun *et al* obtained agreement between their reflectivity data and scaling predictions at small values of momentum transfer.

Dai *et al* [70] have used neutron reflection to study adsorption of the block co-polymer polyacetylene–polyisoprene at the surface of toluene solutions. Polyacetylene (PA) up to a molecular weight of about 2000 may be solubilised in toluene by making AB block co-polymers with polystyrene or polyisoprene (PIP). Not surprisingly, the co-polymer is surface active and there is some indication that it also forms micelles in solution. The determination of the structure of the material both in solution and at the surface is somewhat complicated by the fact that the co-polymer appears to aggregate slowly with time. Once again, the use of different isotopes helped to disentangle possible models of the surface layer. The composition PIP(h)PA(d) in about 2% solution by weight in toluene-d_8 gave a significantly enhanced reflectivity relative to toluene-d_8 on its own, and this was attributed to the formation of a 10 Å layer of polyacetylene at the surface with a layer of polyisoprene extending up to about 50 Å into the solution.

Henderson *et al* [71] have used neutron reflectivity to determine the structure of spread polymethylmethacrylate layers, comparing their results with π–A isotherms on the same polymer samples. The most important result was the determination of the thickness of the layer as a function of pressure. Since the isotherm gives the area per segment, the traditional method of estimating the thickness of the layer is to combine the area per segment with the bulk density. At the limiting surface concentration used by Henderson *et al*, this gave a layer thickness of 8 Å, significantly lower than that obtained from the reflectivity. As for the case of PEO, this was attributed to a distinct roughness of the spread layer, although in the case of PMMA the effect is not as large.

4.1.5. Soap films. When a film is drawn from a solution of surfactants at a suitable concentration, usually below the CMC, it initially drains rapidly and then, depending on the species of the surfactant, the nature of the electrolyte, the electrolyte concentration and the temperature, it will thin to an equilibrium 'black' film with a thickness anywhere in the range 50–1000 Å [72]. The structure of a black film has never been established by a direct experimental method. There is some interest in establishing the structure and in following the rate of drainage in very thin films because of the relation of both to colloidal forces.

An early experiment by Highfield *et al* [15] showed that neutron reflection is sufficiently sensitive for the study of single soap films, although nothing of any value was obtained from this first study. Since then, Lee [53] has studied the different isotopic species of decyltrimethyl ammonium bromide/sodium decanoate aqueous NaBr black

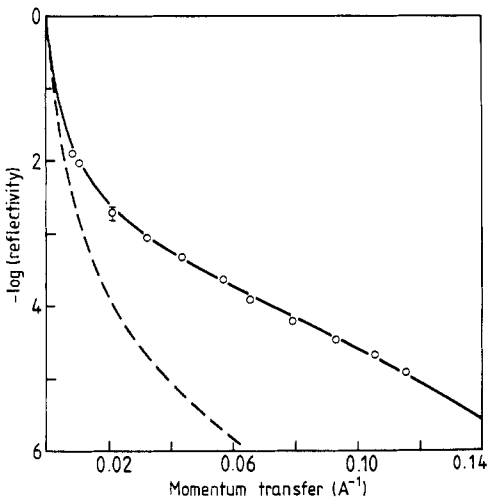

Figure 19. Observed and calculated reflectivity profiles for hexaethylene glycol monododecyl ether ($C_{12}E_6$) adsorbed at the quartz water interface (background subtracted) at its critical micelle concentration. The dashed line is from the clean surface in water not quite perfectly matched to the quartz [73].

films. She has followed the rate of drainage in vertical films over the last 200 Å and determined a final film thickness of 70 ± 2 Å. The reflectivity profiles of the black films contained a significant contribution from non-specular scattering. This was shown to be a result of coupling across the film between the capillary waves on each face. This effect had been observed earlier in light scattering measurements, although not on such a large scale, by Vrij [44]. It suggests that the correct way to interpret reflectivity data would be to include specular and non-specular contributions in full.

4.1.6. Solid–liquid and liquid–liquid interfaces. Both solid–liquid and liquid–liquid interfaces are of great technological importance because of their dominant role in colloid stability. They are also both somewhat inaccessible to study by experimental methods capable of giving unambiguous structural information. It would be of considerable interest to be able to do the same kinds of experiments on the liquid–vapour interface, described above, on adsorption at either of the two interfaces between condensed phases.

The experiment could, in principle, be done in a number of ways. The more direct and the easiest to interpret would be for the neutron beam to be passed into a fairly transparent condensed phase and then to be reflected at the interface between the two media. Suitable transparent solid media would be quartz, sapphire or silicon, all of which have intrinsically interesting surface properties. Transparent liquids are more difficult to find because they often contain protons. The extinction length of neutrons in most proton containing materials is only of the order of mm, whereas what is required at glancing angles is penetration of the order of cm or more so that a sufficient area of surface may be illuminated to give a measurable signal. Even a transparent liquid such as CS_2 is not necessarily suitable for examining, say, the CS_2–water interface because small amounts of protonated or deuterated solvent or solute saturating the CS_2 may be sufficient to reduce the beam to an unusable level.

A second method is to use a thin film or liquid or solid adjacent to the second condensed phase. The neutron beam is then reflected at the thin film–air interface. However, if the scattering length density of the film is matched to air, no reflection will occur at the first interface and the signal will be entirely from the interface of interest. The difficulty with this method is that the contrast match to air can usually only be

achieved with a large fraction of protonated material. For the beam to reach the second interface the thickness of the film must then be reduced to a few microns. This makes the control of the experiment exceedingly difficult, though not impossible. It is not necessary to match the contrast of the thin film to air. If its thickness is within the range where it will give interference fringes, i.e. less than about 4000 Å, the fringes will be modified by the presence of an adsorbed layer at the second interface. Limited information may then be gleaned about adsorption at the second interface. The experimental difficulties in such an arrangement may be even greater than in the previous case.

Lee *et al* [73] have successfully determined the structure of an adsorbed surfactant layer at the quartz–water interface. The surfactant was hexaethylene glycol monododecyl ether ($C_{12}E_6$). The quartz was in the form of Suprasil, an amorphous quartz, polished as smooth as possible. The experiment was done on the D17 instrument where advantage could be taken of the greater transmission of the quartz at long wavelengths.

Figure 19 shows the reflectivity profiles of an adsorbed layer of protonated $C_{12}E_6$ (actually a bilayer) on quartz in an isotopic mixture of H_2O and D_2O approximately contrast-matched to the quartz. For comparison, the profile for the water on its own is also shown in the figure. The adsorbed layer has a remarkably strong effect on the reflectivity. Results from the corresponding experiment on the fully protonated layer adsorbed from D_2O are shown in figure 20. The combination of the data from the two figures was combined to give the most direct 'picture' of the structure of an adsorbed layer at the solid–liquid interface yet obtained by any non-destructive technique. Figure 20 also shows the effect of lowering the coverage to approximately half. If at half coverage the layer were to spread 'uniformly' over the surface the reflectivity profile should change exactly as observed in figure 20. If, on the other hand, the layer were to split into regions where large areas of the surface were bare, then the half-coverage profile would be an average of the profile at full coverge and that of D_2O. 'Uniformly' here means that the size of any island of adsorbate is smaller than the in-plane resolution, about 1 μm in this experiment. A further feature of this experiment is that Lee *et al* were able to follow the adsorption and desorption of the surfactant as a function of pH and thereby demonstrate that the system was at equilibrium.

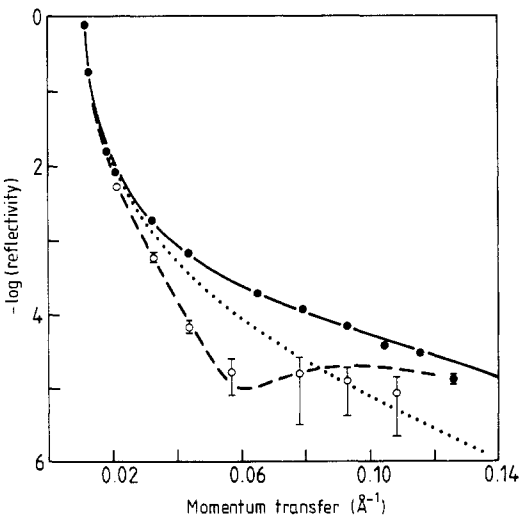

Figure 20. Observed and calculated reflectivity profiles for $C_{12}E_6$ adsorbed from D_2O solution at the quartz–water interface (background subtracted). The profiles are from the maximum coverage (0.75) of $C_{12}E_6$ (● and full curve) (conditions as for figure 19); pure D_2O (dotted curve), and a coverage of 0.4 (○ and broken curve) [73].

Rennie *et al* [74] have done a similar experiment on the adsorption of polyethylene oxide on the same quartz surface. Once again, a remarkably clean signal was obtained, although its magnitude was significantly less than that from the surfactant. One of the difficulties in the study of adsorbed polymer layers is the lack of contrast of most of the layer with the solvent because of the large fraction of solvent incorporated into the layer.

4.2. Solid films

4.2.1. Low-dimensional structures. Materials with low-dimensional structures are of considerable interest because their physical properties can differ radically from those of bulk solids; and multilayer structures are expected to generate a new range of electronic and optical devices (for example quantum well lasers, and materials with new physical properties). To understand the physical properties of such multilayers it is important to determine their layer structure and investigate any interfacial irregularities and defects within the layers.

Harwood *et al* [75] have used neutron reflection to study the properties of a 30 bilayer platinum–carbon multilayer. Neutron reflection provides important information about the nature of the carbon layers, whereas, for example x-ray reflection would be dominated by the platinum. A detailed simultaneous analysis of the interference pattern from the total layer (see figure 21(*a*)), and of the first-order Bragg peak arising from the bilayer structure (see figure 21(*b*)), give a bilayer thickness of 52.6 Å, in good agreement with the layer thickness (26 Å) obtained from the deposition rate. The density of the platinum and carbon layers was determined to be 21.5 and 1.98 g cm^{-1}. The density of the platinum compares well with that of the crystalline material, whereas the carbon layers are some 15% less dense than crystalline carbon, indicating that the carbon layer is amorphous carbon. From the fitting of the reflectivity profiles it was found that the layer–substrate interface is not sharp but varies smoothly over a thickness of some 140 Å. The presence of the density gradient between the multilayer structure and the substrate may result either from diffusion of the deposited atoms into the substrate or from defects on the surface of the substrate.

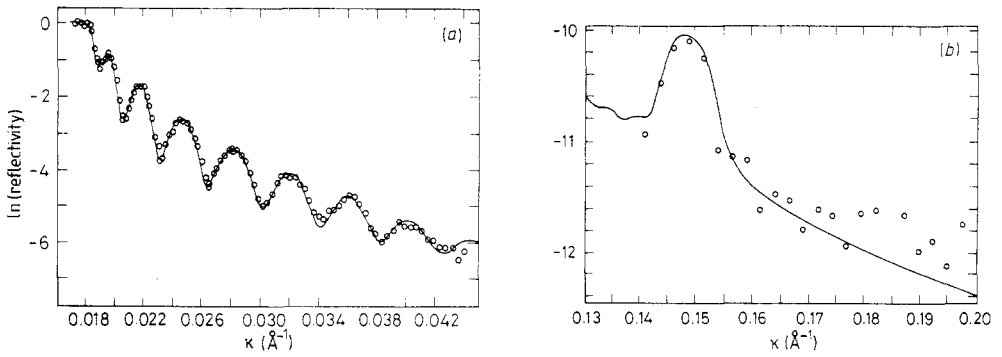

Figure 21. (*a*) Reflectivity measured at $\theta = 0.5$ (○) and the best model fit for a smooth layer–substrate interface (curve); with layer thickness $D = 1215$ Å, intrfacial width $D_1 = 140$ Å, mean layer scattering length density, $\langle p \rangle = 6.45 \times 10^{-6}$ Å^{-2} and substrate scattering length density $p_s = 0.215 \times 10^{-5}$ Å^{-2}. (*b*) Reflectivity measured at $\theta = 3.0°$ (○) and calculated reflectivity for 28 Pt/C bilayers of thickness $d = 42.6$ Å plus a platinum layer of 21.3 Å, with a smooth layer–substrate interface (curve) [75].

In order to understand the optical and electrical properties of low-dimensional semiconductor structures it is important to be able to determine layer thicknesses and densities accurately and to characterise interfacial irregularities.

Ashworth *et al* [76, 77] have investigated single insulating layers of silicon nitride and silicon oxide on silicon, formed by chemical vapour deposition. The analysis of the reflectivity profile from the silicon nitride film gave a layer thickness in good agreement with the normal thickness (2500 Å), whereas the density of the layer was lower than expected (2.38 g cm^{-2} compared with a value for amorphous silicon nitride (Si_3N_4) of 3.44 g cm^{-2}) (see figure 22). Ashworth *et al* postulated that the reduced density is due to a mixture of silicon oxide and silicon nitride arranged on an amorphous lattice. They also observed that the film interfaces are diffuse.

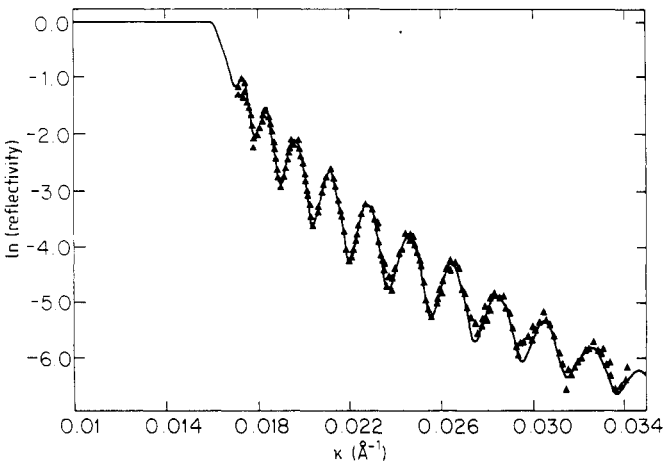

Figure 22. Reflectivity from a silicon nitride film in a silicon substrate at $\theta = 0.5°$ (Δ) data. Curve is a least-squares fit to the data for a film thickness, $d = 2340$ Å, scattering length density $Nb = 0.51 \times 10^{-5}$ and air–layer interface = 180 Å [76].

The silicon dioxide layers were deposited on silicon using plasma-enhanced and plasma-controlled chemical rapid deposition [78]. The layer thicknesses are close to the expected values (1000 and 1300 Å). However, in this case the density of the layer is some 8% and 20% higher than expected for amorphous silicon dioxide. A crystalline film is unlikely and Ashworth *et al* attribute the enhanced density to the presence of nitrogen or a higher oxygen concentration. Both films have diffuse interfaces at the air–film and film–substrate boundaries, and the extent of the interfacial regions varied somewhat from sample to sample.

It is known that hydrogen is important in controlling the electronic properties of semiconductors and in particular the silicon–silicon oxide interface. In amorphous and polycrystalline materials hydrogen passivates dangling bonds, and recently hydrogenation has been found to have advantageous effects on the performance of devices made from single-crystal silicon. The mechanism is not understood and the evidence for the absence or presence of interlayer hydrogen is under debate. Ashworth *et al* [78] have investigated by neutron reflection poly-silicon/silicon oxide layers deposited on silicon and subjected to hydrogenation; the different hydrogenation treatments gave rise to

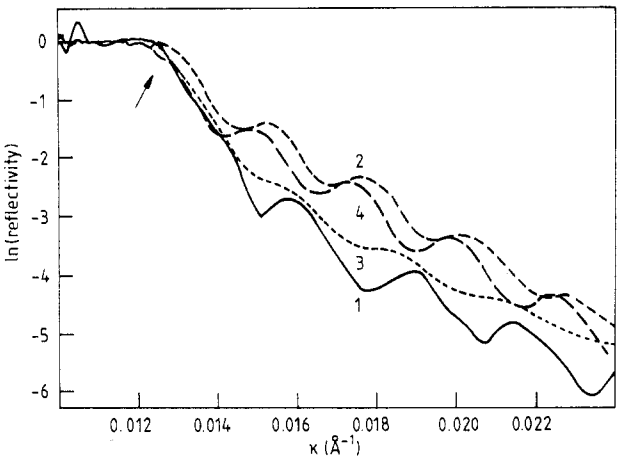

Figure 23. The experimental reflectivity curves for the four samples. The arrow indicates the critical reflection edge. Sample 1, control; sample 2, furnace hydrogenated at 500 °C; sample 3, plasma hydrogenated at 350 °C; sample 4, furnace hydrogenated at 500 °C and plasma hydrogenated at 350 °C [78].

markedly different reflectivity profiles (see figure 23). The samples consisted of a 5000 Å thick silicon oxide layer on silicon with a surface layer of poly-silicon of 2000 Å, and were hydrogenated by plasma and furnace bake treatments. The reflectivity pofile of the untreated sample gave film thicknesses and densities in good agreement with expected values; furthermore the poly-silicon/silicon oxide and silicon oxide/silicon interfaces were sharp and well defined. After hydrogenation the reflectivity profiles changed markedly. The enhanced reflection beyond total reflection indicates that the main difference is that the treated samples have a surface layer of higher scattering length density, consistent with the oxidation of the surface during treatment. The greater damping of the interference fringes stems from a diffuse interface between the poly-silicon and silicon oxide layers, consistent with oxygen diffusion into the poly-silicon. For the plasma treated sample the surface oxidised layer is less dense and the poly-silicon oxide interface is more diffuse; this is explained by the presence of atomic hydrogen which will enhance oxygen diffusion and reduce the scattering length density of the surface layer. A detailed quantitative analysis has been made of the different hydrogenation treatments to support the broad conclusions.

4.2.2. Hard carbon films. There is growing interest in the properties and applications of amorphous hydrogenated carbon films. They are grown from a variety of deposition techniques which include hydrogen plasmas and ion beam methods. The films can be formed in a range of conditions and compositions from soft highly hydrogenated materials to hard low hydrogen content (diamond) films. Much of the potential applications have focused on the low hydrogen content films as anti-abrasion and anti-reflection coatings. Grundy *et al* [79] have used neutron reflection in combination with other techniques to characterise some plasma-deposited films on silicon. The reflectivity profiles of the hard and soft films in this initial study were well described by a single uniform film (see figure 24), and there was no significant composition gradient within the film. The film thicknesses and densities were determined to good accuracy, and independent density measurements enabled the film compositions to be determined. Analysis of interference patterns indicated little interdiffusion at the film–silicon interface and further experiments are planned to examine this in more detail. In conjunction with optical band gap measurements, the neutron reflectivity results have been used to

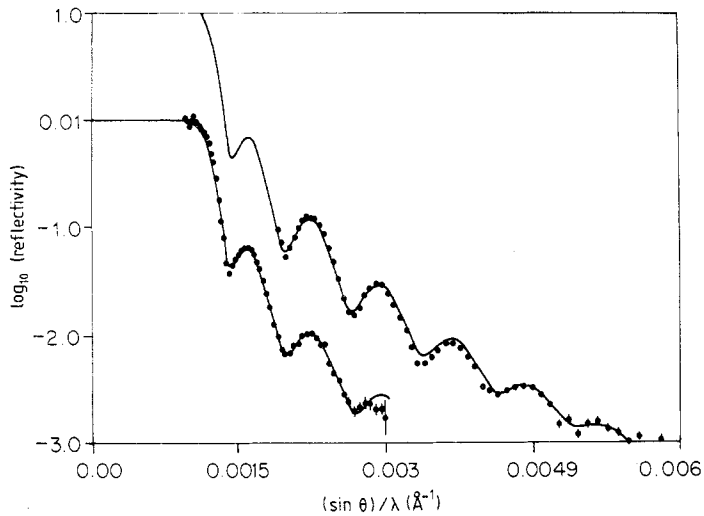

Figure 24. Neutron reflectivity profiles for a CiH film on silicon. Upper curve, glancing angle = 0.7°; lower curve, glancing angle = 0.35°. The upper curve is displaced vertically for clarity. The full curves are model fits to the data [79].

postulate a model for the structure of the film, which consists of the formation of a randomly oriented cluster of fused benzene rings connected by hydrocarbon chains.

4.2.3. Langmuir–Blodgett films. In recent years much attention has been paid to potential application of Langmuir–Blodgett films as well ordered thin films in molecular electronics, microelectronics, integrated optics and microlithography. Langmuir–Blodgett (L–B) films were one of the early chemical systems studied by neutron reflection. Highfield *et al* [14] measured the interference fringes from L–B multilayers of cadmium arachidate-d_{39} on glass, which were the first observation with neutrons of interference fringes from organic layers. The evolution of the reflectivity profile with increasing thickness was analysed for films with 2 to 59 molecular layers. The spacing of the interference fringes gave a measure of the overall film thickness and hence the average thickness of a molecular layer. Using a model which treated the film as a uniform slab, for the 20-layer film (see figure 25), they found an average thickness per layer (24.6 Å) which was less than the observed neutron Bragg spacing (26.7 Å) and the length of the arachidate molecule. This discrepancy was reconciled with an alternative model which incorporated a region of reduced scattering density and a reduction in the thickness of the layers adjacent to the glass substrate. This alternative model gave a good fit to both the interference and Bragg diffraction data multilayers prepared on hydrophobic substrates. In contrast multilayers deposited on untreated glass conformed to the uniform slab model with an average thickness per layer of 24.75 Å.

Despite the potential, the applications of L–B films have been slow to materialise, probably due to a lack of detailed understanding of some of the basic processes involved in their deposition. With this in mind Buhaenko *et al* [80] have used x-ray and neutron diffraction to study the structure and temperature dependence of L–B films of fatty acids and their cadmium salts for different subphase, dipping and substrate conditions. In the neutron studies they chose to use the large differences in scattering between hydrogen and deuterium to study the temperature dependence of AB structures using alternate

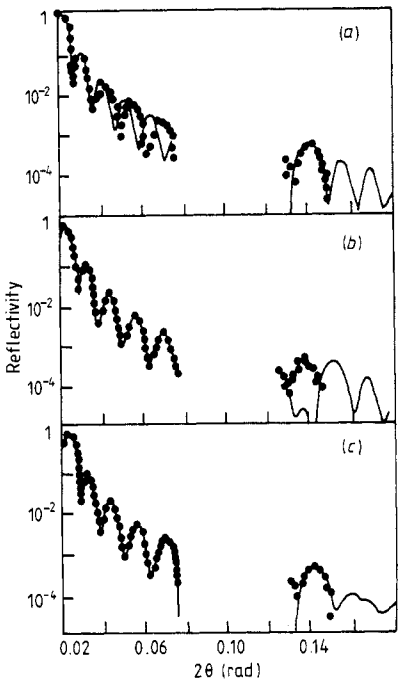

Figure 25. Observed and calculated reflectivity profiles of 20 layers of cadmium arachidate-d_{39} on glass. The layer thickness is assumed to be: (*a*) 26.75 Å; (*b*) 24.5 Å; (*c*) as the model described in the text [14].

hydrogenated and deuterated fatty acid layers. If interlayer mixing occurs it is possible using HHDD and HDHD films to distinguish between two possible types of mixing, single molecule or molecular dimer diffusion. The x-ray measurements on the pure acid show the temperature-dependent transition of the B–C phase (d-spacing changes from 53 to 48 Å) common in the bulk material. The lack of such polymorphism in the neutron results demonstrate that the B–C phase transition takes place with a dramatic rearrangement of the film; there is no neutron diffraction from the C phase in either the HDHD or HHDD films. A similar situation arises from the neutron data for the onset of the 'disordered' phase in the soap films.

Nicklow *et al* [81] have used neutron diffraction to investigate the magnetic structure of L–B films of manganese stearate. The data have been well described using a layered structural model of the multilayer. The neutron results have indicated some overlap of the Mn with the COO groups which were not seen on a previous x-ray study. They discussed the advantages of neutron diffraction in determining the magnetic structure, but assumed that there would be little progress on the case of Mn stearate because the magnetic ordering in the phases is likely to be antiferromagnetic. Since that paper there has, as we will refer to later, been some progress in determining the magnetic structure in thin films and multilayers.

4.2.4. Polymer films. There is much interest in the nature of thin polymer films, and again contrast variation makes neutron reflection a powerful technique for studying many of the current problems in polymer systems such as the nature of thin films, interdiffusion at the interface between different polymers, surface enrichment, and ordering of block co-polymers at interfaces and surfaces. Stamm [82] reported interference in thin polymer films (~200 Å) for polystyrene cast from solution onto glass

substrates. Fernandez [83] and Russell [84] have subsequently reported measurements of the nature of the interface between different polymer systems.

The degree of mixing between polymer components in a binary mixture has profound significance for the mechanical properties of the material, and the time dependence of intermixing can provide important information about the interdiffusion coefficients of the polymer pair (the subject of much current theoretical effort). The process of interdiffusion can be followed right from the start by neutron reflection. Russell *et al* [84] have studied a bilayer consisting of deuterated polystyrene (d-PS) (320 Å) on top of a protonated polystyrene (h-PS) (1120 Å) layer. An analysis of the reflectivity profiles shows good agreement with the expected thickness and bulk density values (see figure

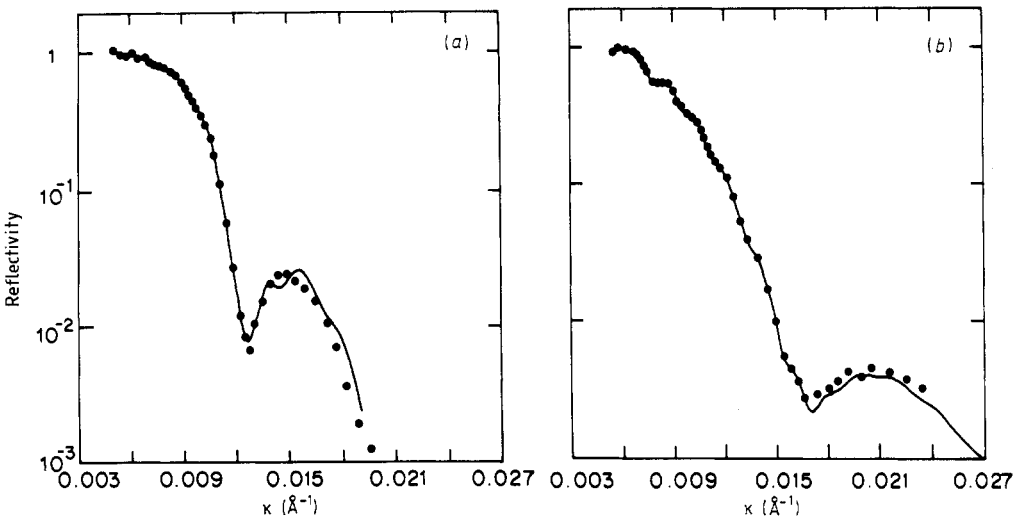

Figure 26. Reflectivity profiles of a bilayer of deuterated and protonated polystyrene on a fused silica substrate: (*a*) reflectivity profile for the sample as prepared; (*b*) reflectivity profile for the sample after heating to 140°C for 5 minutes. The full curves are calculated reflectivity profiles, as described in the text [84].

26). The damping of the interference pattern gives an apparent interfacial thickness between the deuterated and protonated layers of 60 Å. An analysis of the reflectivity profile after annealing at 140°C for 300 s has established that the total thickness of the bilayer remains constant, but that the thickness of the deuterated layer has decreased by 120 Å. The nature of the interface is substantially unaltered by the annealing process. The changes in scattering length density indicate that the deuterated polymer has diffused into the protonated layer, but not vice versa. These observations are consistent with the theories of Brochard and de Gennes [87] who predict, for diffusion times short compared to the repetition time of the slower diffusing component, a sharp interface even if the interface moves by a swelling mechanism.

Fernandez *et al* [83] have investigated the nature of the interface between an immiscible pair of polymers. They have investigated a thin deuterated polymethylmethacrylate (d-PMMA) layer (~200 Å) deposited onto a thick (~8000 Å) protonated polystyrene (h-PS) layer (figure 27). An analysis of the interference pattern, arising predominantly from the PMMA top layer, has established the thickness and density of the d-PMMA film before

and after annealing at 120 °C for 6 h. The interface between the two polymers remains sharp (≤20 Å) throughout. This is contrary to previous predictions. The predominant changes on annealing are that the d-PMMA layer thins (from 200–180 Å) and densifies (ρ = 1.278 g cm^{-3} to ρ = 1.369 g cm^{-3}). A similar densification of the upper layer was reported by Russell *et al* [84]. The origin of the densification is uncertain: it may be due to the change of a rather loosely packed structure formed by the fast removal of solvent during the spinning technique, or because the thermodynamics of thin polymer films is different from the bulk.

The results of Fernandez [83] and Russell [84] were the first extensively reported studies on polymer systems, and have firmly established the value of neutron reflection for studying solid polymer systems. Subsequently studies have been reported [85, 86] on different aspects of thin polymer films. Fernandez *et al* [85] have examined the nature of the interface between the miscible polymer pair deuterated polymethylmethyacylate (d-PMMA) and protonated solution chlorinated polyethylene (h-SCPE) and provided further experimental evidence to support the theory of Brochard and de Gennes [87]. Figure 28 shows the reflectivity profile of the d-PMMA/HSCPE polymer pair before and after annealing at 120 °C for 2 h. The predicted fringes arise from the upper d-PMMA layer and the more closely spaced modulations from interference in the h-SCPE layer. The damping of the fringe pattern is predominantly caused by the interface between the two polymers, which increases slightly from 70 to 90 Å on annealing. The main change on annealing is that the upper d-PMMA layer thins from 970 to 920 Å, consistent with the theory of Brochard and de Gennes.

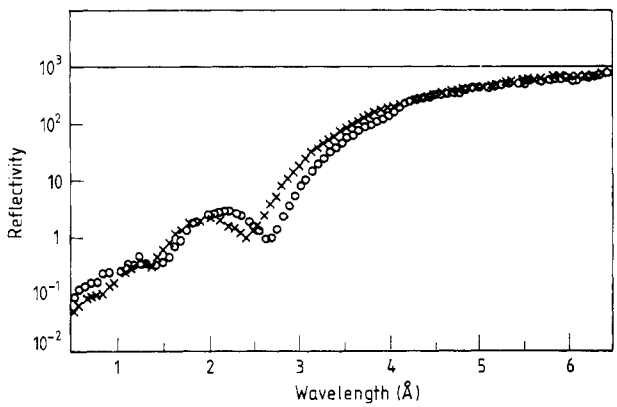

Figure 27. Reflectivity profiles of a bilayer of deuterated polymethyl methacrylate (d-PMMA) and hydrogenous polystyrene (h-PS) on an optical flat: ○, before annealing; ×, after annealing for 6 h at 120 °C followed by storage at room temperature for 18 weeks.

Composto *et al* [86] have attempted to measure surface segregation in a polymer blend containing 10% deuterated polystyrene (d-PS) after thermal treatment. They have observed a well defined interference pattern from a polystyrene (10% d-PS/90% h-PS) film (~3000 Å) on a glass substrate, and have observed changes on annealing. Because of the limited range of κ covered by the experiment they were not able to make a unique determination of any surface enrichment of the d-PS.

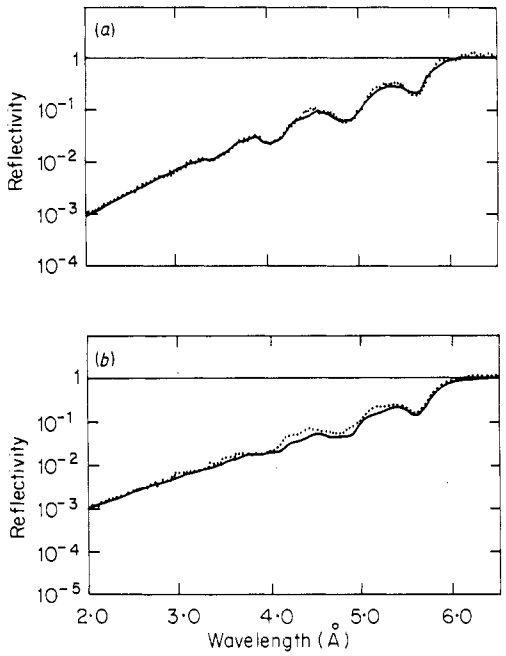

Figure 28. Reflectivity profiles of a bilayer of deuterated polymethyl methacrylate and hydrogenous solution chlorinated polyethylene on an optical flat: (*a*) before annealing; (*b*) after annealing at 120 °C for 2 h. The full curves are calculated profiles as described in the text [85].

4.3. Surface magnetism

For magnetic materials magnetised in the plane of the surface the neutron spin-dependent refractive index gives rise to a spin-dependent reflectivity $R_{\pm}$. The neutron spin reflectivity ratio R_+/R_- has been shown to be a sensitive probe of the surface magnetisation profile. Much of the early interest was in the development of devices for polarising thermal neutrons, which were initially based on thin ferromagnetic films [6, 7]. This work has been extended to multilayers, both bilayers [8, 88, 89] for monochromatic polarisation, and multilayers of the form of band-pass filters (supermirrors) [9, 27, 90, 91–93] in order to widen the range of high reflecting mirror coatings. Although the application of neutron reflection to the production of polarised neutron remains of great importance, attention is now being focused on the application of polarised neutron reflection to the study of surface magnetism.

Felcher [10] was the first to discuss the use of polarised neutron reflection to determine the surface magnetisation of a ferromagnet and presented calculations to show that for nickel the temperature dependence of the magnetisation at the surface of a ferromagnet could be determined to a sensitivity of one dead magnetic layer. Subsequently the technique has been to study the effect of the interface on magnetisation in ferromagnetic films, the effects of reduced dimensionality on the magnetisation in thin films and multilayer, and finally as an absolute and direct measurement of flux penetration in superconductors.

4.3.1. Magnetic multilayers. Some of the earliest measurements were on multilayer systems, where reduced dimensionality, the influence of the interface and coupling between the layers are of interest. Sato *et al* [93] have used polarised neutron diffraction to study the magnetism in multilayers of Fe–SiO: the moment was not substantially changed from the bulk moment of iron. The study of magnetism in systems with reduced dimensionality was the motivation of the work of L–B films of manganese stearate by Nicklow *et al* [81].

More recently Majkrzak *et al* [94, 95, 96] have applied polarised neutron diffraction to the study of a number of interesting magnetic multilayers. Majkrzak *et al* [94, 95] have investigated Fe–Ge multilayers, and figure 29 shows their results for the spin-dependent reflectivities $R_{\pm}$ of a Fe–Ge multilayer. They have established from x-ray diffraction that the Fe layers are microcrystallites oriented with a [110] direction normal to the plane of the film and randomly rotated within that plane, and that the Ge layers are amorphous. The analysis of the polarised neutron diffraction data shows a significant reduction in the Fe moment, which can be accounted for by an Fe–Ge alloyed region adjacent to the Fe and Ge layers. They conclude in this case that, although an accurate determination of the magnetisation profile is possible, it is difficult when interdiffusion masks the effects of alloying and reduced dimensionality.

4.3.2. Flux penetration in superconductors. Although the discussion so far has centred on the measurement of magnetisation profiles in ferromagnetic systems some of the early important experiments on measuring magnetic perturbations close to a surface have been to measure the magnetic field penetration into a superconductor [18, 97, 98].

We write the spin-dependent refractive index $n_{\pm}$ as

$$n_{\pm}(z) = 1 - (\lambda^2/2\pi)\big(b/v \pm c(B(z) - H)\big) \tag{4.5}$$

where H is the magnetic field parallel to the surface, and assume for a superconductor, for H less than the critical magnetic flux field H_{c1}, that there is an exponential magnetic induction into the material of the form

$$B(z) = H\exp(-z/\Lambda) \tag{4.6}$$

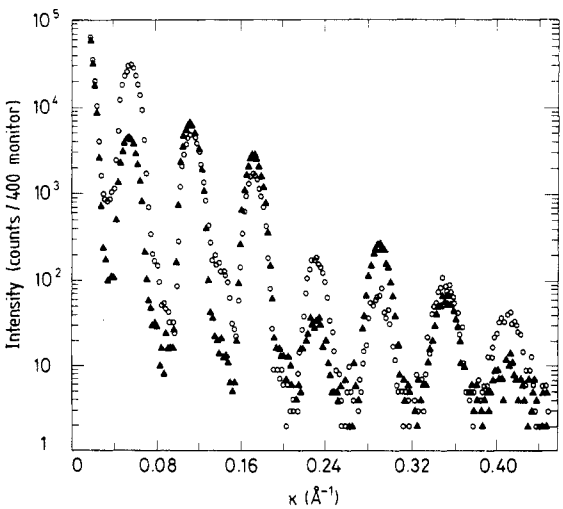

Figure 29. Polarised neutron diffraction for a Fe–Ge multilayer: ○, spin up; △, spin down [94].

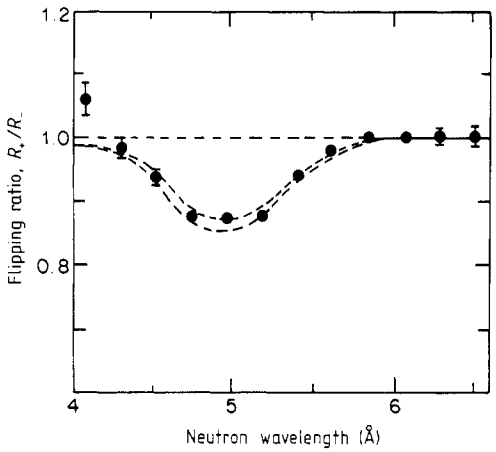

Figure 30. The spin reflectivity ratio (R_+/R_-) for a niobium film at 4.6 K and 500 Oe, $\theta = 0.34°$. The broken curves are calculations, in ascending order, for $\Lambda = 380$ and 480 Å [97].

where Λ is the magnetic field penetration depth. The spin-dependent reflectivity can provide a sensitive, direct and absolute measurement of the penetration depth Λ in superconductors.

The first measurement by Felcher *et al* [97] was on a thin film of the type 2 superconductor niobium (figure 30). Measurements were made at different magnetic fields and temperatures, and an extrapolated value of Λ at $T = 0$ of 410 ± 40 Å was obtained. This was in good agreement with theoretical estimates and other measurements interpreted through the Ginzburg–Landau theory, and furthermore Λ showed the expected temperature dependence. Similar measurements on a film of pure lead, a type 1 superconductor, showed the sharp cross-over from superconductivity to normal state above H_c.

Measurements on a lead (92%)–bismuth (8%) alloy [96], an incipient type II superconductor, show a much smoother transition from the superconducting to normal state, consistent with the existence of an intermediate magnetic phase. However it has not yet been possible to attribute this unambiguously to the predicted surface sheath of superconductivity predicted to occur between H_{c2} and H_{c3}.

More recently polarised neutron reflection has been applied by Felici *et al* [99] and Mansour *et al* [100] to the determination of the penetration depth in the 'new breed' of high-temperature superconductors. Samples of $YBa_2Cu_3O_{7-x}$, prepared in quite different ways, have been studied; the sample investigated by Felici *et al* [99] was the polished surface of a compacted pellet manufactured by normal powder techniques, whereas the sample of Mansour *et al* [100] was a thin epitaxial film with the *c* axis of the superconductors orthorhombic structure perpendicular to the film surface. The two measurements give somewhat different results, the values of Λ for the former being 250 Å and the latter 1400 Å. However, it is a parameter for which it has been surprisingly difficult to get a consensus over a range of measurement techniques, and it is most likely that the differences reported from polarised neutron reflection measurements represent sample-dependent effects (such as surface modification due to polishing) rather than any fundamental difficulties on differences in interpretation.

4.3.3. Ferromagnetic surfaces. A number of interesting ferromagnetic systems of technological relevance have been investigated by polarised neutron reflection. Sputtered iron oxide films are promising materials for high-density magnetic recording. Parkin *et*

al [101] have investigated the differences between Fe_3O_4 and γ-Fe_2O_3 thin films (~2600 Å in thickness), the latter showing characteristics (such as higher coercive fields) more ideal for magnetic recording. The data from the Fe_3O_4 films was interpreted as a uniform magnetisation except for an outermost layer ~ 30 Å, the extent of the surface roughness; the values of magnetisation obtained are in agreement with other measurements but are only a fraction of that of bulk Fe_3O_4. In contrast to the Fe_3O_4 reflectivity data, the γ-Fe_2O_3 data showed clearly that the magnetisation profile was not uniform. The data were interpreted by a model using a surface magnetically dead layer (~150 Å) and an extensive interfacial region in which a reduced moment increased linearly into the bulk interior of the film.

Metallic alloy glasses have been extensively studied and are now finding technological applications. For example, rapidly quenched alloy ribbons based on the transition metals Fe, Co and Ni are inherently magnetically soft and have been developed as transformer laminates. In many of the applications the large surface to volume ratio for ribbons requires a knowledge of the magnetisation near to the surface.

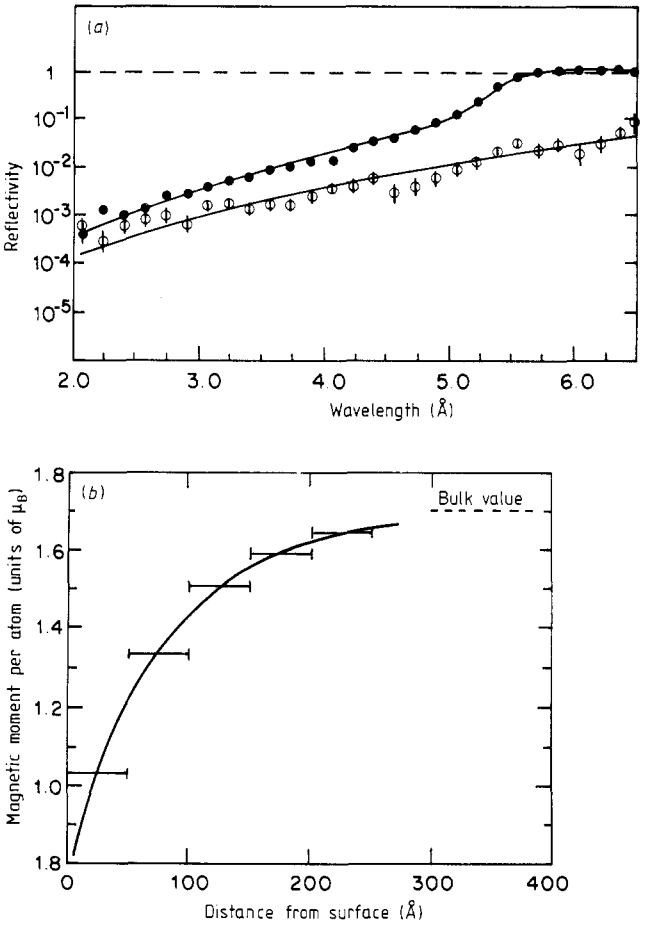

Figure 31. (*a*) The spin-dependent reflectivities in R_+ (●) and R_- (○) for a metallic glass ribbon ($Fe_{78}B_{13}Si_9$). The full curves are the calculated reflectivities described in the text. (*b*) Magnetisation profile in the surface of the metallic glass ribbon, derived from the calculated reflectivity profiles [102].

Ivison *et al* [102] have used polarised neutron reflection to determine the surface magnetisation in a commercial metallic glass ribbon of METGLASS 260552 (an alloy of $Fe_{78}B_{13}Si_9$), the spin-dependent reflectivities $R_{\pm}$ being shown in figure 29. The analysis of this preliminary data gives a bulk moment per atom of 1.7 μB, corresponding to 2.2 μB per iron atom, some 13% larger than expected from bulk magnetisation measurements. An important additional feature is that the spin-dependent reflectivity profiles are consistent with a decrease in magnetisation near the surface. The data have been fitted (figure 31) assuming an exponential variation of magnetisation with the surface value approximately half the bulk value, and a magnetic coherence length of about 80 Å.

4.3.4. Ultra-thin ferromagnetic films. The magnetic properties of ultra-thin epitaxial films of ferromagnetic materials are of increasing theoretical and experimental interest. Felcher [18] has discussed the sensitivity of polarised neutron reflection in the measurement of the magnetisation in extremely thin (a few monolayers) ferromagnetic films. It was demonstrated that by sandwiching the film between the substrate and a thicker overlayer a significant enhancement of the spin dependence of the reflectivity can be obtained. It was shown that for a magnetic layer of thickness d_2, with a scattering density Nb_2 deposited onto a substrate of scattering density Nb_1 and covered by an overlayer of thickness d_1 and the same scattering density Nb_1, then for small d_2 the spin reflectivity ratio can be expanded in terms of d_2. Retaining only linear terms in d_2

$$R_+/R_- \sim 1 + (8d_2k_0/Nb_1)\sin(2d_1k_1) \tag{4.7}$$

where k_0, k_1 are the perpendicular components of the neutron momentum in vacuum and medium 1. The sine term in the equation is the enhancing factor; if no overlayer were present then the spin reflectivity ratio would differ from unity only through the higher terms in d_2 which have been ignored in equation (4.7). For a 20 Å ferromagnetic layer, with a copper substrate and overlayer of about 100 Å, the enhancement is 50–100 times.

Willis and co-workers [103–105] have successfully exploited this enhanced sensitivity in a series of investigations of ultra-thin epitaxial layers of cobalt and iron grown on copper ⟨100⟩ single-crystal substrates, and covered by a copper overlayer. The normally hexagonal close packed (HCP) cobalt and body-centred cubic (BCC) iron are both grown as face-centred cubic (FCC) onto ⟨100⟩ copper substrate.

The epitaxial thin films (7–20 Å thick) of FCC cobalt [103] on Cu ⟨100⟩ exhibit strong ferromagnetism with a moment per atom $\mu = 1.8\,\mu$B, close to that of bulk HCP cobalt, and show no significant variation of the moment with film thickness down to a single monolayer. The early measurements on ultra-thin FCC iron film [103] showed no in-plane magnetisation, in contrast to polycrystalline BCC iron films of a similar thickness which gave a moment similar to the bulk moment of BCC iron of 2.2 μB. Willis *et al* have discussed these results in terms of calculated moments for these metastable magnetic states and discuss various possible interpretations, such as a strong magnetic anisotropy normal to the film surface, or the lack of any real moment in the FCC iron films.

Further measurements by Willis *et al* [104] have been used to confirm the magnetic anisotropy of the FCC iron films, i.e. that the FCC iron films prefer to align their spins normal to the surface in contrast to FCC cobalt films. Polarised neutron reflection measures a spin-dependent reflectivity only when the magnetisation has a component

in the plane of the film, any magnetisation normal to the surface giving a null effect. Willis *et al* [104] showed for a 3-monolayer FCC iron film sandwiched between copper ⟨100⟩ at 4 K an increasing spin reflectivity ratio with an increase of applied field from 60 through 1000 to 4000 Oe. This increase in spin reflectivity ratio is interpreted as an increase in the in-plane magnetisation when the applied magnetic field is sufficiently strong to orient the spins into the plane of the film. From an assumed saturation field of 2–5 kOe the spin reflectivity ratio gives a moment per atom of 1–1.5 μB, in agreement with spin polarised photoemission measurements. The observed anisotropy in FCC iron films has been discussed in relation to the structural variations in the films [102].

In the most recent polarised neutron reflection measurements (figure 32) [105] Willis *et al* have shown that ultra-thin FCC iron films grown epitaxially onto copper ⟨100⟩ can exist in a high-moment magnetically ordered state with an average magnetic dipole moment per atom close to bulk BCC iron, but that this state is unstable with respect to an increase in either film thickness or growth temperature. This implies that small alterations in the structure of FCC iron films can significantly alter their magnetic properties.

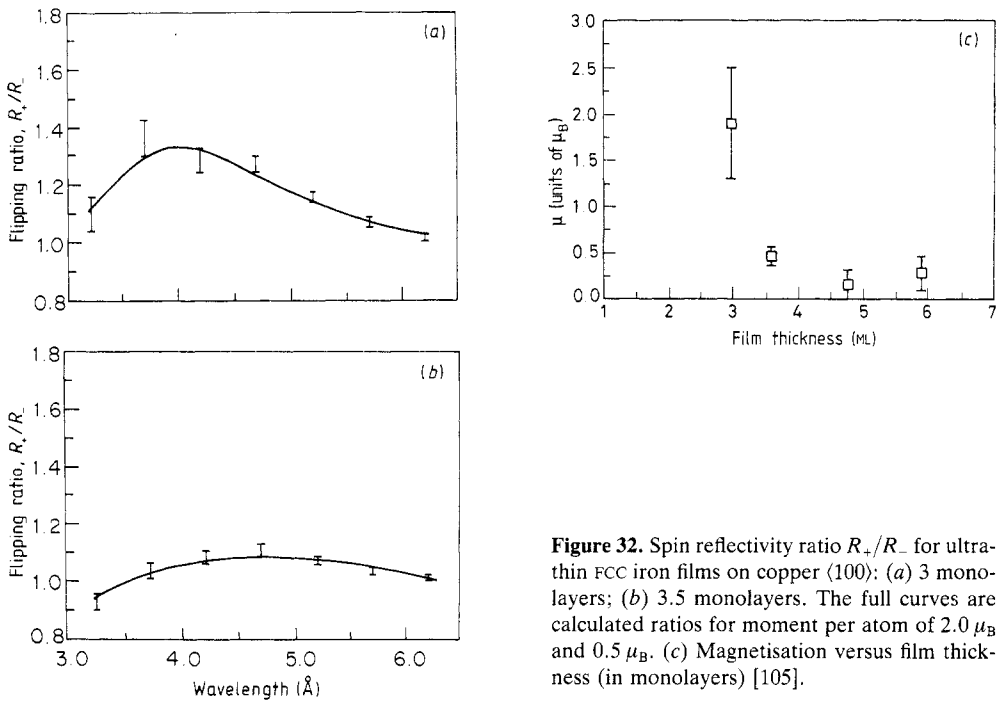

Figure 32. Spin reflectivity ratio R_+/R_- for ultra-thin FCC iron films on copper ⟨100⟩: (*a*) 3 monolayers; (*b*) 3.5 monolayers. The full curves are calculated ratios for moment per atom of 2.0 μ_B and 0.5 μ_B. (*c*) Magnetisation versus film thickness (in monolayers) [105].

References

[1] Klein A G and Werner S A 1982 *Rep. Prog. Phys.* **46** 259
[2] Fermi E and Zinn W 1946 *Phys. Rev.* **70** 103
[3] Fermi E and Marshall W 1947 *Phys. Rev.* **71** 666
[4] Koester L and Steyrl A 1977 *Neutron Physics* (Berlin: Springer)

[5] Maier-Leibnitz H and Springer T 1963 *Reactor Sci. Tech: J. Nucl. Energy* **17** 217
[6] Hayter J B, Penfold J and Williams W G 1978 *J. Phys. E: Sci Instrum.* **11** 454
[7] Abrahams K, Patynski W, Stecher-Rasmussen F and Waring E 1966 *Nucl. Instrum. Methods* **45** 293
[8] Lynn J W, Kjems J K, Passell L, Saxena A M and Schoenborn B P 1976 *J. Appl. Crystallogr.* **9** 454
[9] Mezei F 1976 *Commun. Phys.* **1** 81
[10] Felcher G P 1981 *Phys. Rev.* B **24** 1995
[11] Bally D, Todireau S, Ripeanu B and Belloni M G 1982 *Rev. Sci. Instrum.* **33** 916
[12] Jones I R and Bartolini W 1953 *Rev. Sci. Instrum.* **34** 28
[13] Hayter J B, Highfield R R, Pullman B J, Thomas R K, McMullen A I and Penfold J 1981 *J. Chem. Soc. Faraday. Trans. I* **97** 1437
[14] Highfield R R, Thomas R K, Cummins P G, Gregory D P, Mingins J, Hayter J B and Scharpf O 1987 *Thin Solid Films* **99** 165
[15] Highfield R R, Humes R P, Thomas R K, Cummins P G, Gregory D P, Hayter J B, Mingins J and Scharpf O 1984 *J. Coll. Interface Sci.* **97** 105
[16] Bradley J E, Lee E M, Thomas R K, Willatt A J, Gregory D P, Penfold J, Ward R C and Waschkowski W 1988 *Langmuir* **4** 821
[17] Lee E M, Thomas R K, Penfold J and Ward R C 1989 *J. Phys. Chem.* **93** 381
[18] Felcher G P, Gray K E, Kampwirth R T and Brodsky M P 1986 *Physica* B **136** 59
[19] Felcher G P, Hilleke R D, Crawford R K, Haumann J, Kleb R and Ostroswki G 1987 *Rev. Sci. Instrum.* **58** 609
[20] Penfold J, Ward R C and Williams W G 1987 *J. Phys. E: Sci. Instrum.* **20** 1411
[21] Felici R, Penfold J, Ward R C and Williams W G 1988 *Appl. Phys.* A **45** 169
[22] Farnoux B 1985 *Proc. Conf. Neutron Scattering in the Nineties* (Vienna: IAEA)
[23] *ISIS Annual Report* 1988 RAL-88-050, 1987 RAL-87-050
[24] Goldberger M L and Seitz F 1947 *Phys. Rev.* **71** 294
[25] Lekner J 1987 *Theory of Reflection* (Dordrecht: Martinus Nijhoff)
[26] Penfold J, Ward R C and Williams W G 1987 *Rutherford Appleton Laboratory Report* RAL-87-014
[27] Hayter J B and Mook H A 1989 *J. Appl. Crystallogr.* **22** 35
[28] Born M and Wolf E 1970 *Principles of Optics* (Oxford: Pergamon)
[29] Heavens O S 1955 *Optical Properties of Thin Films* (London: Butterworth)
[30] Anders H 1967 *Thin Films in Optics* (London: Focal Press)
[31] Névot L and Crocé P 1980 *Phys. Appl.* **15** 761
[32] Cowley R A and Ryan T W 1987 *J. Phys. D: Appl. Phys.* **20** 61
[33] Felici R and Penfold J 1989 unpublished results
[34] Penfold J 1988 *Rutherford Appleton Laboratory Report* RAL-88-088
[35] Crowley T L 1984 *DPhil Thesis* Oxford University
[36] Crowley T L, Thomas R K and Willatt A J 1990 to be published
[37] Als-Neilsen J 1985 *Z. Phys.* **64** 411
[38] Brochaud E, Farnoux B, Sun X, Daoud M and Jannink G 1986 *Europhys. Lett.* **2** 315
[39] Sinha S K, Sirota E B, Garott S and Stanley H B 1988 *Phys. Rev.* B **38** 2297
[40] Jaccobsson R 1966 *Progress in Optics* vol V, ed. E Wolf
[41] Braslau A, Pershan P S, Swislow G, Ocko B M and Als-Neilsen J 1988 *Phys. Rev.* A **38** 2457
[42] Hamilton W A, Klein A G, Opat G I and Timmins P A 1987 *Phys. Rev. Lett.* **58** 2770
[43] Sauro J, Fankuchen I and Wainfan N 1963 *Phys. Rev.* **132** 1544
[44] Vrij A 1964 *J. Colloid Sci.* **19** 1
[45] Bindell J B and Wainfan N 1970 *J. Appl. Crystallogr.* **3** 503
[46] Hayter J B, Penfold J and Williams W G 1976 *Nature* **262** 569
[47] Unpublished results 1983: Neutron research facilities at the ILL high-flux reactor
[48] *Los Alamos Report* 1988 LA-11301-C
[49] Stamm M, Reiter G and Huttenbach S 1990 *Physica* B submitted
[50] van Well A A and Fredrihze H 1989 *Delft Report* no IRI-132-15
[51] Jones T J L and Williams W G 1977 *Rutherford Appleton Laboratory Report* RAL-77-029
[52] Rennie A R, Crawford R J, Lee E M, Thomas R K, Crowley T L, Roberts S, Qureshi M S and Richards R W 1989 *Macromolecules* **22** 3466
[53] Lee E M 1989 *DPhil Thesis* Oxford
[54] Penfold J, Shackleton C, Hughes-Davies T T, Lee E M, Thomas R K and Rennie A R 1990 in preparation
[55] Braslau A, Deutsch M, Pershan P S, Weiss A H, Als-Neilsen J and Bohr J 1985 *Phys. Rev. Lett.* **54** 144

[56] Elworthy P H and Mysels K J 1966 *J. Colloid Sci.* **21** 331
[57] Chattoraj D K and Bridi K S 1984 *Adsorption and the Gibbs Surface Excess* (New York: Plenum)
[58] Enderby J E and Neilson G W 1979 *Water: A Comprehensive Treatise* vol 6, ed F Franks (New York: Plenum) 1
[59] Tanford C J 1972 *J. Phys. Chem.* **76** 3020
[60] Penfold J, Lee E M and Thomas R K 1989 *Mol. Phys.* **68** 33
[61] Rennie A R, Penfold J and Thomas R K 1990 to be published
[62] Lee E M, Simister E A, Thomas R K and Penfold J 1989 *J. Physique. Coll.* **50** C7 Suppl.10 75
[63] Gaines G L 1966 *Insoluble Monolayers at Liquid–Gas Interfaces* (New York: Wiley Interscience)
[64] Grundy M J, Richardson R M, Roser S J, Penfold J and Ward R C 1988 *Thin Solid Films* **159** 43
[65] Fleer G J and Lyklema J 1983 *Adsorption from Solution at the Solid/Liquid Interface* ed G D Parfitt and C H Rochester (New York: Academic)
[66] Kuzmenka D J and Granick S 1988 *Macromolecules* **21** 779
[67] Scheutjens J M H M and Fleer G J 1980 *J. Phys. Chem.* **84** 180
[68] Sun X, Bouchaud E, Lapp A, Farnoux B, Daoud M and Jannink G 1988 *Europhys. Lett.* **6** 207
[69] Ober R, Paz L, Taupin C, Pincus P and Boileau S 1983 *Macromolecules* **16** 50
[70] Dai L, White J W, Kerr J, Thomas R K, Penfold J and Aldissi M 1989 *Synth. Met.* **28** D69
[71] Henderson J, Richards R W, Penfold J and Thomas R K 1990 in preparation
[72] Ivanov I B 1988 *Thin Liquid Films* (New York: Marcel Dekker)
[73] Lee E M, Thomas R K, Rennie A R, Penfold J, Cummins P G and Staples E J 1989 *Chem. Phys. Lett.* **162** 196
[74] Rennie A R, Lee E M and Thomas R K in preparation
[75] Harwood N H, Messoloras S, Stewart R J, Penfold J and Ward R C 1988 *Phil. Mag.* B **58** 217
[76] Ashworth C D, Messoloras S, Stewart R J, Wilkes J G, Baldwin I S and Penfold J 1989 *Phil. Mag. Lett.* **60** 37
[77] Ashworth C D, Messoloras S, Stewart R J, Wilkes J G, Baldwin I S and Penfold J 1989 *J. Phys. D: Appl. Phys.* **22** 1862
[78] Ashworth C D, Messoloras S, Stewart R J and Penfold J 1989 *J. Semicond. Sci. Technol.* **4** 1
[79] Grundy M J, Richardson R M, Roser S J, Beamson G, Brennan W J, Howard J, O'Neil M, Penfold J, Shackleton C and Ward R C 1989 *Thin Solid Films* **159** 43
[80] Buhaenko M R, Grundy M J, Richardson R M and Roser S J 1988 *Thin Solid Films* **159** 253
[81] Nicklow R M, Pomerantz M and Segmuller A 1981 *Phys. Rev.* B **23** 1081
[82] Stamm M and Majkrzak C F 1987 *Am. Chem. Soc. Polymer Preprints*
[83] Fernandez M L, Higgins J S, Penfold J, Ward R C, Shackleton C and Walsh D J 1988 *Polymer* **29** 1923
[84] Russell T P, Karim A, Mansoor A and Felcher G P 1988 *Macromolecules* **21** 1890
[85] Fernandez M L, Higgins J S, Penfold J, Ward R C, Shackleton C and Walsh D J 1990 *Polymer Commun.* submitted
[86] Composto R J, Stein R S, Kramer E J, Jones R A L, Mansoor A, Karim A and Felcher G P 1988 *Proc. Int. Conf. on Neutron Scattering, Grenoble* (Amsterdam: North-Holland) p 434
[87] Brochard F and de Gennes P G 1983 *Phys. Chem. Hydrodynamics* **4** 313
[88] Saxena A M and Schoenbaun B P 1977 *Acta Crystallogr.* A **33** 809
[89] Majkrzak C F and Passell L 1985 *Acta Crystallogr.* A **41** 41
[90] Gukasov A G, Ruben V A and Bedrizova M N 1977 *Sov. Tech. Phys. Lett.* **3** 52
[91] Yamada S, Ebisawa T, Achiwa N, Akiyoshi T and Okamoto S 1978 *Annual Report, Res. React. Inst. Kyoto Univ.* **11** 8
[92] Schelten J and Mika K 1979 *Nucl. Instrum. Methods* **160** 287
[93] Sato M, Abe K, Endoh N and Hayter J B 1980 *J. Phys. C: Solid State Phys.* **13** 3563
[94] Majkrzak C F 1986 *Physica* B **136** 69
[95] Majkrzak C F, Axe J D and Boni P 1985 *J. Appl. Phys.* **57** 3657
[96] Majkrzak C F *et al* 1988 *J. Appl. Phys.* **63** 3447
[97] Felcher G P, Kampwirth R T, Gray K E and Felici R 1984 *Phys. Rev. Lett.* **52** 1537
[98] Felcher G P, Felici R, Kampwirth R T and Gray K E 1985 *J. Appl. Phys.* **57** 3789
[99] Felici R, Penfold J, Ward R C, Olsi E and Matacotta C 1987 *Nature* **329** 523
[100] Mansoor A, Hilleke R O, Felcher G P, Laibowitz R B, Chandhari P and Parkin S S P 1988 *Proc. Int. Conf. on Neutron Scattering, Grenoble* (Amsterdam: North-Holland) p 867
[101] Parkin S S P, Sigsbee R, Felici R and Felcher G P 1985 *Appl. Phys.* **57** 3771
[102] Ivison P K, Cowlam N, Gibbs M R J, Penfold J and Shackleton C 1989 *J. Phys.: Condens. Matter* **1** 3655

[103] Bland J A C, Pescia D and Willis R F 1987 *Phys. Rev. Lett.* **58** 1244
[104] Willis R F, Bland J A C, Schwarzacker W 1988 *J. Appl. Phys.* **63** 8
[105] Schwarzacker W, Allison W, Willis R F, Penfold J, Ward R C and Egelhoff W F Jr 1989 *Solid State Commun.* **71** 563